UNCERTAINTY QUANTIFICATION IN SEISMIC IMAGING

by

Iga Pawelec

© Copyright by Iga Pawelec, 2018

All Rights Reserved

A thesis submitted to the Faculty and the Board of Trustees of the Colorado School of Mines in partial fulfillment of the requirements for the degree of Master of Science (Geophysics).

Golden, Colorado

Date _____

Signed: _____
Iga Pawelec

Signed: _____
Dr. Paul C. Sava
Thesis Advisor

Golden, Colorado

Date _____

Signed: _____
Dr. John Bradford
Professor and Head
Department of Geophysics

ABSTRACT

To make informed decisions, one has to consider all available knowledge about the assessed problem. An important part of the decision-making process is understanding uncertainties and how they influence the outcome. In seismic exploration, many decisions are based on interpretations of seismic images, which are affected by multiple sources of uncertainty. Thus, image uncertainty quantification is an important, albeit challenging task.

In this thesis, I focus on two uncertainty sources that affect seismic imaging: data uncertainty and velocity uncertainty. I quantify the seismic data uncertainty using theoretical analysis applied to two field experiments with repeated shots. My analysis reveals that amplitude distributions for each data sample as a function of time and position are not Gaussian and that the uncertainty of a seismic event is proportional to its mean amplitude. I also find that seismic events excited by the source are highly repeatable, but small changes of the source position impact the amplitude response, highlighting the importance of geometry repeatability for the lapse studies.

Velocity uncertainty also has a large impact on image uncertainty, as it affects reflector positioning and the focusing of seismic events. By examining two subsalt imaging scenarios with geological uncertainty caused by the salt body physical properties, I demonstrate that image uncertainty, expressed as a function of the image amplitude or as a function of the reflector location, is the largest under the salt: the image amplitude distributions are two times broader under the salt than away from it. The confidence index maps are a useful tool to convey the information about image amplitude uncertainty to an interpreter, while the location uncertainty reveals uncertain directions and is affected by acquisition geometry.

The main challenges facing uncertainty quantification in seismic imaging include integration of different sources of uncertainty and reducing the computational cost of the analysis. My analysis leads to recommendations about possible approaches towards these challenges,

with emphasis on using sparsity to reduce the dimensionality of the problem.

TABLE OF CONTENTS

ABSTRACT iii

LIST OF FIGURES vii

LIST OF ABBREVIATIONS xi

ACKNOWLEDGMENTS xii

DEDICATION xiii

CHAPTER 1 INTRODUCTION 1

1.1 Uncertainty quantification - why bother? 1

1.2 Uncertainty quantification workflow 1

1.3 Probability density functions 2

1.3.1 Mean, variance and covariance 4

1.3.2 Information and entropy 5

1.4 Gaussian distributions 6

1.5 Seismic imaging 7

1.6 Uncertainty sources and assumptions in seismic imaging 8

1.7 Challenges 10

CHAPTER 2 UNCERTAINTY QUANTIFICATION FOR LAND SEISMIC ACQUISITION 11

2.1 Introduction 12

2.2 Field experiments 14

2.2.1 Experiment A: 100 shots repeated at a single location 14

2.2.2 Experiment B: 10 shots repeated at 10 nearby locations 16

2.3 Methodology 20

2.4 Uncertainty quantification results 22

2.5 Data repeatability 27

2.6 Discussion and conclusions 33

CHAPTER 3 THE IMPACT OF VELOCITY UNCERTAINTY ON THE QUALITY OF THE SEISMIC IMAGE 41

3.1 Introduction 41

3.2 Methodology 47

3.3 Image uncertainty 51

3.3.1 Velocity vs image 51

3.3.2 PDF-based analysis 53

3.3.3 Location uncertainty 58

3.4 Discussion and conclusions 58

CHAPTER 4 CONCLUSIONS AND RECOMMENDATIONS 65

4.1 Conclusions 65

4.2 Recommendations 67

REFERENCES CITED 69

LIST OF FIGURES

Figure 1.1 Schematic representation of Bayesian inversion. Information is captured as probability density functions, which can be characterized by their mean and covariance. 4

Figure 1.2 Schematic representation of reverse time migration. D_S and D_R are the source wavelet and the recorded receiver data, respectively. W represent the corresponding wavefields and R is an image created after applying the imaging condition $I.C.$ 8

Figure 2.1 Acquisition geometry for the wired (up) and wireless system (down). . . . 14

Figure 2.2 An example of a shot recording for 100 experiments. The red and green dots indicate points for which I analyze the reflection amplitude and position. The blue crosses indicate where I form amplitude distributions. . 15

Figure 2.3 Receiver gather with car noise (top) and after median filtering along the experiment axis (bottom). Note that a large portion of noise is removed, but filtering residuals are present, e.g. for shot index 100. 17

Figure 2.4 An example of data recorded on wired system for 10x10 experiment. The region between red lines indicates where wireless data are available. Note that reflection signal is not clearly visible on this raw shot record. . 18

Figure 2.5 (a) An example shot recorded on the wireless system and (b) the same shot recorded on the wired system. Note the difference in data readability, especially for the slow events. 19

Figure 2.6 Marks on the road indicating the position of Vibroseis plate for experiment B. The distance between consecutive shot location is on the order of 1-2m. 21

Figure 2.7 (a) The mean amplitude and (b) the standard deviation for experiment A, computed using equations 2.1 and 2.2. 24

Figure 2.8 (a) The mean amplitude and (b) the standard deviation for 10 shots recorded on the wired system. 25

Figure 2.9 (a) The mean amplitude and (b) the standard deviation for 10 shots recorded on the wireless system. 26

Figure 2.10 PDF's for data points indicated by blue crosses on Figure 2.2. Distribution shapes are not Gaussians. 28

Figure 2.11 Trace fidelity computed using equation 2.3. Channel reliability increases with offset. 29

Figure 2.12 From left to right: a trace 215 extracted from shot 2 (experiment A), its mean and standard deviation as functions of time. 30

Figure 2.13 Reflection time uncertainty (left) and amplitude uncertainty (right) for events indicated on Figure 2.2. The kinematic repeatability is high, while the amplitude fluctuates. 31

Figure 2.14 Different ranges of repeatability index for experiment B_1. Seismic events excited by the source are highly repeatable, but some of them are aliased. 34

Figure 2.15 Different ranges of repeatability index for B_2. Dark lines indicate dead channels. Seismic events are highly repeatable and non-aliased. 35

Figure 2.16 Comparison of amplitude as a function of shot index for $t = 770$ms, $x = 620$m for experiment B_1 (top) and B_2 (bottom). The stair-like pattern is reflecting changes in the source location, but the behavior of the amplitude for the two systems is not consistent after the shot 60. . . . 36

Figure 2.17 Comparison of amplitude as a function of shot index for $t = 243$ms, $x = 680$m for experiment B_1 (top) and B_2 (bottom). The stair-like pattern is reflecting changes in the source location and the behavior of the amplitude for the two systems is consistent except for the spike of noise for shot 60. 37

Figure 3.1 Velocity model with two scatterers, used to demonstrate the effects of too slow and too fast velocity on image focusing (Figures 3.2 and 3.3). . . 44

Figure 3.2 (a) The image of a scatterer formed with the whole velocity model 2% too slow, (b) image formed with correct velocity and (c) image with the whole velocity model 2% too fast. Note that for the scatterer on the right, the pattern due to incorrect velocity is harder to interpret than for the scatterer on the left. This is due to the presence of a salt body over right scatterer (Figure 3.1). 45

Figure 3.3 (a) The image of a scatterer formed with the whole velocity model 10% too slow, (b) image formed with correct velocity and (c) image with the whole velocity model 10% too fast. 46

Figure 3.4 (a) The velocity model used to generate data for the salt inclusion scenario. The yellow line is a line of receivers on the surface. The green and blue dots are subsediment and subsalt sources, respectively. (b) Data generated from the model above used for imaging in the salt inclusion scenario. 48

Figure 3.5 (a) The velocity model used to generate data for the unknown salt boundary scenario. The yellow line is the line of receivers on the surface. The green and blue dots are subsediment and subsalt sources, respectively. (b) Data generated from the model above used for imaging in the salt boundary scenario. 49

Figure 3.6 ℓ_2 distance of the velocity difference vs ℓ_2 distance of the image difference for the salt inclusion scenario (Figure 3.4). The distances are normalized on a common scale for both scenarios. 51

Figure 3.7 ℓ_2 distance of the velocity difference vs ℓ_2 distance of the image difference for the unknown salt boundary scenario (Figure 3.5). The distances are normalized on a common scale for both scenarios. 52

Figure 3.8 (a) Image generated with the true velocity and (b) the mean image computed from the amplitude PDFs for the salt inclusion scenario. 54

Figure 3.9 (a) Image generated with the true velocity and (b) the mean image computed from the amplitude PDFs for the unknown salt boundary scenario. 55

Figure 3.10 PDF of amplitude between 1000 realizations for the subsediment source (green) and the subsalt source (blue) for the salt inclusion scenario. Note that the range of amplitudes is much broader for the subsalt source. . 56

Figure 3.11 PDF of amplitude between 1000 realizations for the subsediment source (green) and the subsalt source (blue) for the unknown salt boundary scenario. Note that the range of amplitudes is much broader for the subsalt source. 57

Figure 3.12 (a) The standard deviation map, computed from 1000 images for the salt inclusion scenario. (b) The confidence index computed using equation 3.2. 59

Figure 3.13 (a) The standard deviation map, computed from 1000 images for the unknown salt boundary scenario. (b) The confidence index computed using equation 3.2. 60

Figure 3.14 (a) The location PDF corresponding to the source under the sediments and (b) the location PDF corresponding to the source under the salt for the inclusion scenario. Note that (a) is very well constrained to the 12m x 12m region, whereas (b) is broader, occupying 50m x 50m region, so its uncertainty is higher. 61

Figure 3.15 (a) The location PDF corresponding to the source under the sediments and (b) the location PDF corresponding to the source under the salt for the unknown salt boundary scenario. Note that (a) is very well constrained to the 25m x 25m region, whereas (b) is broader, occupying 60m x 60m region, and has higher uncertainty. 62

LIST OF ABBREVIATIONS

Reverse Time Migration . . . . . RTM

Uncertainty Quantification . . . . . UQ

Full Waveform Inversion . . . . . FWI

Center for Wave Phenomena . . . . . CWP

ACKNOWLEDGMENTS

This thesis is inspired by many interesting discussions I had with my advisor, Paul Sava and his quest to do the right thing in estimating data uncertainty. I really appreciate Paul's support, both in the matters related to my studies and outside them, as well as challenging me to become a better researcher. Without his assistance, I would not have come such a long way in my two years at Mines.

There are multiple people in the Department of Geophysics (GP) and Center for Wave Phenomena (CWP) who deserve my gratitude for different ways in which they assisted me. My fellow CWP students were always willing to help out with software trouble and brainstorm problems together. I would like to offer my special thanks to Daniel Rocha, Ivan Lim and Thomas Rapstine, who helped me more times than I can count. GP and CWP staff, Michelle Szobody, Joana Perez and Dawn Umpleby, were always accessible to sort out administrative issues or just talk. Diane Witters, along with Paul Sava, are the reason for my improved technical writing skills. I learned to be a better presenter thanks to the feedback from multiple people offered during my sponsor meeting rehearsals. I appreciate the lessons I have learned either from taking classes or just conversing with CWP faculty: Ilya Tsvankin, Roel Snieder and Jeffrey Shragge.

I want to thank all the CWP sponsors who provide funds for students like me to conduct their research. I am grateful for their presence and continued interest in our research, expressed by regular attendance at our annual consortium meetings.

I would like to thank the members of my committee, Whitney Trainor-Guitton, Michael Wakin and Roel Snieder for making time to chat about research challenges.

Finally, I would like to thank my family and friends for the continued support in pursuing my dreams away from my home country.

For my beloved brother, Filip.

CHAPTER 1

INTRODUCTION

1.1 Uncertainty quantification - why bother?

"... in this world nothing can be said to be certain, except death and taxes," said Benjamin Franklin, in a letter to Jean-Baptiste Leroy. Indeed, uncertainty seems to be an inherent part of our lives and is also present in data that are the basis for scientific inference. There are a couple of reasons. First, one cannot fully control the environment in which data are collected. Even in a laboratory, it is quite impossible to eliminate all outside influences that may affect the experiment. Second, instruments used for measurements have limited accuracy. Third, scientists supervising experiments are just human and can make mistakes. In summary, one cannot know everything with perfect accuracy, which gives rise to the need to account for uncertainty. Of course, science does not end with data acquisition; the big challenge is to infer what data can tell about the problem of interest. To answer this question, one needs to understand what caused the data to have certain features; and there might be many possible explanations, i.e. many different theoretical models of the system that produces the observed data. However, the exact workings of this system, physical or otherwise, are not always known, which again points out the need to understand uncertainty. Uncertainty quantification (UQ), which aims to assess the reliability of scientific inference, is emerging as an independent field of study. If the uncertainty is quantified, one knows not only what the answer likely is, but also to what degree the answer can be trusted.

1.2 Uncertainty quantification workflow

A comprehensive uncertainty quantification encompasses many aspects, including the following, highlighted at a U.S. Department of Energy workshop (2009, p.121).

- uncertainty of measurements

- ignorance (unknown unknowns)
- limitations of theoretical models
- limitations of numerical representations of these models
- limitations of the accuracy and reliability of computations, approximations, and algorithms
- uncertainty due to the human factor

Ideally, the results of uncertainty quantification yield 1) a quantitative assessment of the reliability of scientific inference, 2) a list of all uncertainty sources, 3) a list of sources that are accounted for in the assessment and 4) a list of assumptions made during the assessment. However, providing such results may be challenging due to the existence of *unknown unknowns* (Sullivan, 2015), the parameters that do influence behavior of a system without our knowledge.

There are two main types of uncertainty. *Aleatoric uncertainty* refers to the uncertainty of inherently variable phenomenon. *Epistemic uncertainty* pertains to the case when the system under study is deterministic (its behavior can be predicted exactly), but there is not enough information about all factors influencing the outcome. This type of uncertainty can be further subdivided into model form uncertainty (meaning that the model describing the system behavior is incomplete or lacking in some way) and parametric uncertainty that arises from the lack of knowledge about true parameter values. An example of aleatoric uncertainty may be the fate of a single radioactive nucleus whereas a seismic image formed with inaccurate velocities has an epistemic uncertainty.

1.3 Probability density functions

An important component of uncertainty quantification is the theoretical framework underlying the analysis. The choice of framework may depend on our knowledge about the

problem. If the only information about the quantity of interest is that it lies in certain interval with equal probability for all values inside this interval, the appropriate tool is interval analysis. The degree of uncertainty can then be simply described by the length of the interval. Uncertainty quantification in this framework is equivalent to the worst case uncertainty scenario (Sullivan, 2015). An alternative, heavily favored in geophysics, is the probabilistic framework based on the Bayesian inference (Tarantola and Valette, 1982a,b; Duijndam, 1988; Tarantola, 1984; Gouveia and Scales, 1998; Tarantola, 2005). The fundamental concept in this framework is the *probability density function (PDF)*. PDFs are defined for continuous random variables, i.e. variables which can take any value over the continuum (e.g. any combination of real numbers). PDFs inform how probabilities accumulate at different parts of a parameters space. Let $f(x)$ denote a probability density function defined over the set $\mathcal{X}$. The following properties must be satisfied:

$$\int_{-\infty}^{\infty} f(x)dx = 1 \tag{1.1}$$

$$f(x) \geq 0 \tag{1.2}$$

The probability of occurrence for the event X such that $a \leq X \leq b$ is defined as:

$$P(X) = \int_a^b f(x)dx. \tag{1.3}$$

Equation 1.3 shows that the probability of any individual point is 0. Since $f_{\mathcal{X}}(x)$ is a *density* function, its units are probability per volume, where volume is defined over the set $\mathcal{X}$.

PDFs provide the most complete description of any statistical phenomena one might be interested in (Tarantola, 2005). In the Bayesian framework, PDFs are used to capture states of information (see Figure 1.1). Prior information about model parameters consists of interpreter knowledge, aided by experience and information from sources independent of observed data, about what the model should be. Prior information about data captures their a-priori uncertainty. Data and model parameters are related through theoretical relationships that may also be uncertain. When the prior information is combined with theory, one

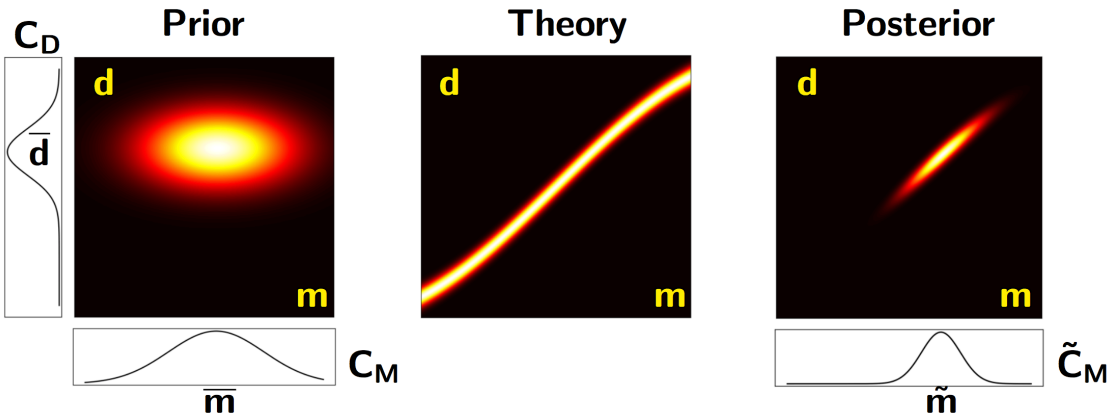


Figure 1.1: Schematic representation of Bayesian inversion. Information is captured as probability density functions, which can be characterized by their mean and covariance.

achieves a refined, posterior state of information. An in-depth description of the Bayesian inversion framework is presented by Tarantola (2005).

In general, PDFs are highly multi-dimensional objects and impossible to compute and store for large scale problems; therefore, one needs to use different parameters capturing the essential character of PDFs instead.

1.3.1 Mean, variance and covariance

The mean is a parameter defining the center of the distribution and can be computed for the multidimensional PDF as:

$$\bar{\mathbf{x}} = \int_{\mathcal{X}} \mathbf{x} f(\mathbf{x}) d\mathbf{x}. \tag{1.4}$$

The mean is quite sensitive to the data outliers. An outlier is a datum that significantly differs from the rest of the collected data. The treatment of outliers depends on interpreter's knowledge about the reason for extreme data values and has to be addressed in the uncertainty assessment.

The variance σ^2 or standard deviation σ are measures of the PDF dispersion. Variance is defined as:

$$\sigma^2 = \int_{\mathcal{X}} \|\mathbf{x} - \bar{\mathbf{x}}\|^2 f(\mathbf{x}) d\mathbf{x}. \tag{1.5}$$

In statistics, a small variance indicates that the PDF is concentrated around the mean.

A generalized version of variance is the covariance, defined as a tensor product:

$$C(\mathbf{x}) = \int_{\mathcal{X}} (\mathbf{x} - \bar{\mathbf{x}})(\mathbf{x} - \bar{\mathbf{x}})^T f(\mathbf{x}) d\mathbf{x}. \tag{1.6}$$

The covariance is always semi-positive definite, and thus it has real, non-negative eigenvalues. The largest eigenvalues and corresponding eigenvectors indicate the orientation of the highest uncertainty. An alternative way of interpreting the covariance may be to look at its norm:

$$\|C\|_2 = \sqrt{\lambda_{\max}(C^T C)}, \tag{1.7}$$

where $\lambda_{\max}$ is the largest eigenvalue of $C^T C$. A large norm would correspond to relatively uninformative (i.e., quite broad) distribution (Sullivan, 2015).

Depending on the problem, one may choose different parameters as proxies for uncertainty. The covariance provides the most information, but cannot be fully formed for problems with large number of parameters as its size is n^2, where n is the model size. In such cases, one may want to explore only the variance or standard deviation.

1.3.2 Information and entropy

The notion of information may seem intuitive, but there are many mathematical perspectives for understanding it (Lombardi et al., 2016). The most widely-used mathematical formulation of information was introduced by Shannon (1948). The amount of information generated by the occurrence of $\mathbf{x} \in \mathcal{X}$ is defined as:

$$I(\mathbf{x}) = -\log(f(\mathbf{x})), \tag{1.8}$$

and measures the surprise value of observing $\mathbf{x}$. Entropy $H(\mathbf{x})$ is the expected information:

$$H = -\int_{\mathcal{X}} f(\mathbf{x}) \log(f(\mathbf{x})) d\mathbf{x}. \tag{1.9}$$

Entropy can be interpreted as a measure of uncertainty. If the distribution $f(\mathbf{x})$ is very "spread out", observing a particular $\mathbf{x}$ has high surprise value, thus it carries a lot of information (Sullivan, 2015).

Information entropy could be a useful uncertainty proxy in the systems for which PDFs are well known. In geophysics that is generally not true, and thus variance or covariance are a better choice for uncertainty proxy.

1.4 Gaussian distributions

Among theoretical distributions, multivariate Gaussians are one of the most widely used and studied (Anderson, 1958). Gaussians provide an accurate description of many random phenomena. Furthermore, according to the central limit theorem, the normalized sum of independent random variables tends towards Gaussian, irrespective of original distributions of said variables. The multivariate Gaussian distribution can be defined as:

$$f_{\mathcal{X}}(x) = \frac{1}{\sqrt{(2\pi)^n \det C}} \exp\Big(-\frac{1}{2}(\mathbf{x}-\bar{\mathbf{x}})^T C^{-1}(\mathbf{x}-\bar{\mathbf{x}})\Big), \tag{1.10}$$

where C is covariance matrix.

Multivariate Gaussians are widely used in geophysics. One of the reasons is that assuming Gaussian distributions leads to the objective function known from deterministic inversions. If prior and theory distributions are Gaussian and the problem is linear, a-posteriori distribution is guaranteed to be Gaussian as well. Finding the maximum a posteriori model (MAP) is then equivalent to minimizing the following objective function:

$$2J = \underbrace{(\mathbf{Gm}-\overline{\mathbf{d}})^T \mathbf{C_D^{-1}} (\mathbf{Gm}-\overline{\mathbf{d}})}_{\text{data fitting}} + \underbrace{(\mathbf{m}-\overline{\mathbf{m}})^T \mathbf{C_M^{-1}} (\mathbf{m}-\overline{\mathbf{m}})}_{\text{model shaping}}, \tag{1.11}$$

where $\mathbf{G}$ is the forward modeling operator, while $\mathbf{C_D^{-1}}$ and $\mathbf{C_M^{-1}}$ are covariances corresponding to distributions. Let $\mathbf{C_d}$ denote data covariance and $\mathbf{C_T}$ denote theory uncertainty covariance. For a linear problem, these two combine as: $\mathbf{C_d} + \mathbf{C_T} = \mathbf{C_D}$. Thus, $\mathbf{C_D}$ characterizes the data and theory PDFs whereas $\mathbf{C_M}$ characterizes the to model PDF.

The analytical formula for the posterior mean is:

$$\tilde{\mathbf{m}} = (\mathbf{G}^T \mathbf{C_D}^{-1} \mathbf{G} + \mathbf{C_M}^{-1})^{-1} (\mathbf{G^T C_D}^{-1} \overline{\mathbf{d}} + \mathbf{C_M}^{-1} \overline{\mathbf{m}}) \tag{1.12}$$

The uncertainty is captured by the posterior model covariance:

$$\tilde{\mathbf{C}}_{\mathbf{M}} = (\mathbf{G}^T \mathbf{C_D}^{-1} \mathbf{G} + \mathbf{C_M}^{-1})^{-1} \tag{1.13}$$

To summarize, Gaussian distributions allow us to use analytic formulas for the mean and covariance of the posterior distribution, a further argument in favor of using them to capture all uncertainties of physical experiments. However, if the true distributions differ from Gaussians significantly, assuming Gaussianity may lead to incorrect interpretation of the solution to an inverse problem.

1.5 Seismic imaging

With advances in acquisition and processing techniques as well as due to the rapidly expanding computing power, the amount of information that can be inferred from seismic data increases significantly. An important application of seismic is delineating the structural image of the subsurface. Knowledge about the presence and the extent of geological structures and stratigraphic sequences is a key to understanding where hydrocarbons may accumulate. A structural image can be inferred from seismic data after careful processing and migration which collapses diffractions and relocates seismic reflection events to their true position in depth.

Over the years, many imaging algorithms have been developed (Claerbout and Doherty, 1972; Stolt, 1978; Larner and Beasley, 1987; Hill, 1990; Gray and May, 1994; Hill, 2001; Gray et al., 2001; Verschuur and Berkhout, 2011; Berkhout, 2012; Xue et al., 2015; Zhou et al., 2018). The state of the art procedure, that can be applied to complex geological settings, is reverse time migration (RTM) (Baysal et al., 1983; Loewenthal and Mufti, 1983; McMechan, 1983; Levin, 1984). In essence, RTM imaging can be summarized in two steps, as illustrated in Figure 1.2. First, one has to simulate the source wavefield by injecting the wavelet at source location and the receiver wavefield by injecting time reversed data at receivers. Second, an imaging condition, most commonly zero-lag time cross-correlation, is applied, since one wants to capture the moment when the source wavefield, originating from

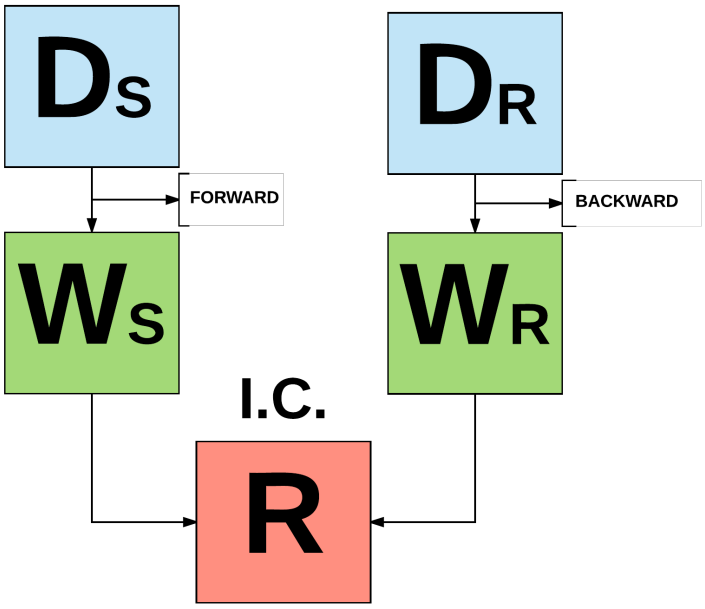


Figure 1.2: Schematic representation of reverse time migration. D_S and D_R are the source wavelet and the recorded receiver data, respectively. W represent the corresponding wavefields and R is an image created after applying the imaging condition $I.C.$

the source, excites the receiver wavefield, originating from seismic discontinuities. The image defined that way is large when wavefronts "meet" in space (which usually happens at seismic interfaces) and zero otherwise.

1.6 Uncertainty sources and assumptions in seismic imaging

As discussed earlier, crucial elements of the UQ workflow are identification of uncertainty sources and assumptions made in the analysis. The main sources of uncertainty in seismic imaging are:

- Geometry uncertainty - inaccurate coordinates of source and receiver positions are part of data uncertainty. Source positions are injection points for source wavelet and receiver positions are injection points for time reversed data in seismic imaging. Since GPS coordinates are usually known with high accuracy, the impact of this type of uncertainty source on a seismic image is small.

- Source signature - the wavelet is source data and thus, it is a part of data uncertainty. The source wavelet is not always known (e.g. for explosive source) and has to be estimated from data. The wavelet uncertainty is relatively small and has a minor effect on a seismic image.

- Data noise - all signal registered by the receivers that is not excited by a seismic source causes data uncertainty. This signal includes, but is not limited to environmental factors and instrumentation noise. I discuss data uncertainty and its potential impact on seismic imaging in Chapter 2.

- Data processing - processing steps taken prior to imaging change raw data uncertainty as they can affect the signal amplitude and kinematics. The impact of data processing on a seismic image may vary, but some procedures, such as, static corrections can potentially affect the positioning of structures on a seismic image.

- Parametric uncertainty - uncertainty related to velocity, anisotropy and density is a part of theory uncertainty. Since the density does not affect the traveltimes, errors in velocity and anisotropic parameters have much more detrimental effect on the quality of a seismic image. Chapter 3 treats particular flavors of velocity uncertainty and their imprint on a seismic image.

- Numerical uncertainty - the numerical accuracy of the wavefield propagator is limited. The associated uncertainty falls within the category of theoretical uncertainty, but its impact on an image is minor.

In RTM, one usually makes the following assumptions:

- Single scattering - data contain only first reflections and diffractions. This means that all other seismic events, such as head waves, direct waves, surface waves, ghosts and multiples, have to be removed prior to imaging. Failure to do so may result in an image with fake structures.

- Physics of wave propagation is accurately described by the chosen wave propagator. For example, if one choses an acoustic wave equation, any S waves events present in data have to be removed to avoid creating fake structures.

1.7 Challenges

Uncertainty quantification in seismic imaging is a challenging problem, for multiple reasons. First, as discussed before, there are many contributing factors, and all of them are difficult to account for. Second, seismic data are often collected as 3D volumes covering large areas. Due to the sheer size of data, solving an inverse problem related to them is computationally expensive. Since it is impossible to explicitly form the posterior covariance matrix, one may settle on sampling the posterior distribution using techniques such as Monte Carlo Markov chain. However, such techniques require multiple iterations of forward modeling (counted in thousands), which are prohibitively expensive for seismic data. Therefore, one needs to introduce further assumptions to make the problem computationally tractable, while still providing valuable insight for a seismic interpreter and providing information for the assessment of a potential prospect.

In this work, I examine two sources of uncertainty in seismic imaging: data noise and velocity uncertainty. In Chapter 2, I discuss uncertainty in raw land seismic data based on two field experiments and make recommendations about the uses in assessing imaging uncertainty. In chapter 3, I quantify the image uncertainty due to model uncertainty, expressing it in two ways: uncertainty of the image pixel value and uncertainty of the location of a specific event. Finally, chapter 4 summarizes lessons learned and provides future outlook and suggestions for dealing with challenges presented by quantifying the uncertainty of a seismic image.

CHAPTER 2

UNCERTAINTY QUANTIFICATION FOR LAND SEISMIC ACQUISITION

Noise is an inherent feature of seismic data, especially in land acquisition. Due to the presence of noise, observations can be treated as random variables with associated uncertainty. An accurate estimate of data uncertainty is important for data interpretation and also for imaging and tomography. For challenging inverse problem, like full waveform inversion, an accurate estimate of data uncertainty can lead to robust qualitative estimates of posterior uncertainty, and also guide the selection of key parameters, e.g. the regularization strength. Uncertainty estimation can be a difficult task for seismic data because not enough repeat measurements are available to estimate reliable statistics.

In this chapter, I use two field experiments to quantify seismic data uncertainty and short-term repeatability of seismic data. Experiment A consists of 100 shots repeated at the same location, giving insight into the amplitude distributions of seismic data as a function of time and position. Experiment B consists shots repeated in groups of 10 at 10 closely spaced points, recorded on two independent systems (wired and wireless) with different spatial sampling, allowing for their comparison with the objective of finding optimal acquisition settings. Furthermore, experiment B gives insight into sensitivity of time-lapse repeatability to small changes in source location. In both experiments, I find that the uncertainty for coherent seismic events in data is proportional to their amplitude. The distributions characterizing the main events in experiment A differ from Gaussians. While the uncertainty associated with the wireless system is higher than for the wired system, the repeatability of seismic events excited by the seismic source is at the same level, with the added benefit of finer spatial sampling that enables better understanding of the data. Changes in source locations are clearly visible in the amplitude response, highlighting the importance of geometry repeatability for time-lapse studies.

2.1 Introduction

Seismic data provide a wealth of information about geological structures, fluid content and physical properties of the subsurface. The information is captured by the traveltime and the amplitude of seismic reflections. To make valid inferences from data, it is important to understand their uncertainty. Although wave propagation is deterministic in nature, i.e., if the medium is known, traveltimes and amplitudes can be uniquely determined. The signal recorded during field acquisition is a superposition of wave phenomena triggered by the seismic source together with the ambient noise.

Repeatability is an important concept for time lapse monitoring, where one seeks to quantify the change in seismic amplitudes related to changes in elastic moduli (Hughes, 1998; Landrø, 2001; Lumley, 2001). Much effort goes into acquisition design to find a setup that maximizes repeatability between the surveys (Poggiagliolmi et al., 1998; Naess, 2006; Houck, 2007). I use a field experiment to discuss the impact on seismic amplitudes of changing the position of the seismic source by a small fraction of the wavelength. However, acquisition geometry repeatability is not the only factor affecting the data. Ambient noise, which may differ between the surveys, and changes to the survey site, such as new sediments on a sea floor or different soil saturation on land, together with imperfectly repeated source signature, also leave an imprint on data (Landrø, 1999).

I seek to evaluate the uncertainty of seismic data, especially with regard to repeatability that is not caused by changes of the medium. I exploit data from the two field experiments (described in detail later) with repeated measurements at the same or nearby location to quantify seismic data uncertainty. Primary sources of uncertainty for both experiments are the instrumentation noise (uncertainty in source signature, sensitivity and coupling of geophones), ambient noise (traffic, background seismicity, wind) and small changes to the experimental environment caused by ground compaction due to repetitions of a Vibroseis source at the same location. I describe the uncertainty in terms of mean amplitude and standard deviation. The ratio of standard deviation to the absolute value of a mean amplitude

quantifies the short-term repeatability of seismic data. As discussed in Chapter 1, standard deviation is a measure of data dispersion. When compared to the mean amplitude, standard deviation represents the percent change in amplitude through experiments.

To infer the properties of the subsurface from seismic data, one generally needs to solve an inverse problem. Recall from Chapter 1 that one way of solving an inverse problem is to use the probabilistic Bayesian framework (Tarantola, 2005), which relies on combining prior information about model and data with theoretical relationship between them to achieve a refined, posterior state of information. Alternatively, one can use the deterministic framework that aims to minimize a specific objective function. Information about data uncertainty may be incorporated as data prior in the Bayesian framework. For example, Osypov et al. (2008) solve a tomographic problem in the Bayesian framework to quantify the posterior uncertainty. In the deterministic framework, uncertainty information can be used in the regularization term. The data regularization term is especially important for strongly non-linear problems, such as full waveform inversion (Tarantola and Valette, 1982a; Pratt, 1999; Virieux and Operto, 2009).

The data prior, captured by the data probability distribution, can be particularly problematic to characterize, due to the time and cost involved in seismic acquisition. Multiple measurements are usually not available to statistically analyze data and quantify their uncertainty. Instead, noise is commonly assumed to be Gaussian, with fixed standard deviation. It is a pragmatic choice in the absence of additional information, as multivariate Gaussian distributions are well studied (Anderson, 1958), their parametrization is easy to interpret in terms of probability and they provide an accurate description of many random processes. However, if the true distribution significantly differs from Gaussian, assuming Gaussianity may lead to wrong conclusions about the inverse problem solution.

In order to assess these assumptions, I use data from a field experiment to evaluate data distributions and the associated statistics as a function of time and position. Since both experiments are conducted within a short period over a non-producing area, changes

in elastic moduli of the medium are not expected except in the immediate vicinity of the seismic source, thus allowing the quantification of data uncertainty caused by uncontrolled environmental causes.

2.2 Field experiments

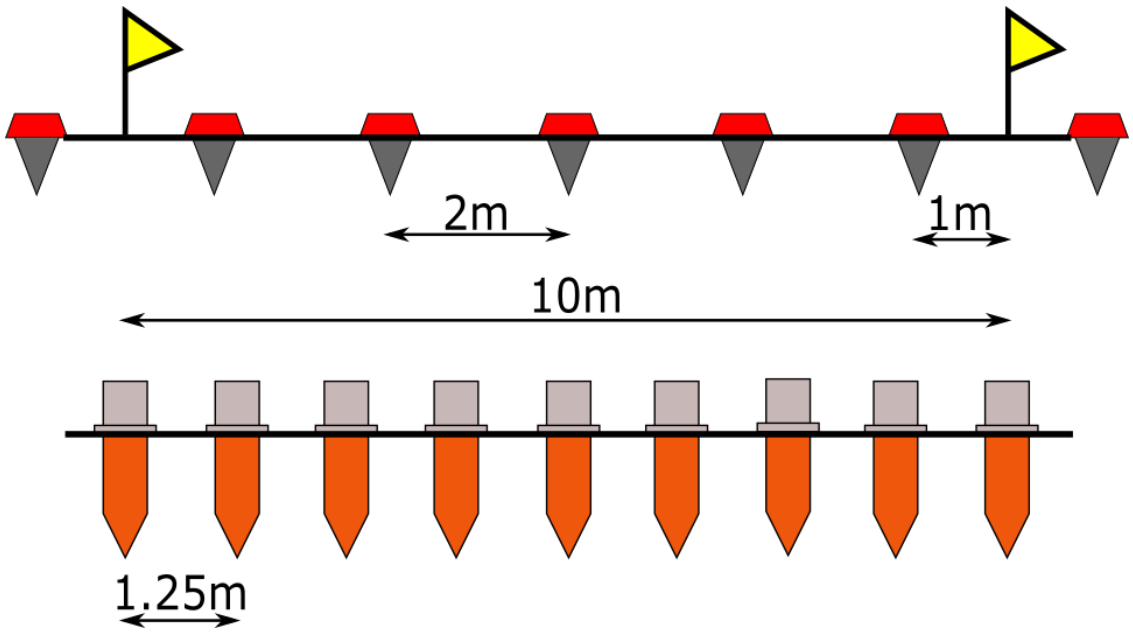


Figure 2.1: Acquisition geometry for the wired (up) and wireless system (down).

In this chapter I analyze data collected during the Colorado School of Mines Geophysical Field Camp in Pagosa Springs in 2016 and 2017, in two separate field experiments. For clarity, I call these field experiments A and B. The following sections detail relevant acquisition details and the specific lessons to be learned from each experiment.

2.2.1 Experiment A: 100 shots repeated at a single location

Repeating the same shot multiple times at the same location allows one to form amplitude distributions for every data sample in time and space. The specific objectives of this experiment are to verify if the amplitude distributions are Gaussian, quantify the data uncertainty and analyze the repeatability of seismic reflections in terms of its amplitude and traveltimes.

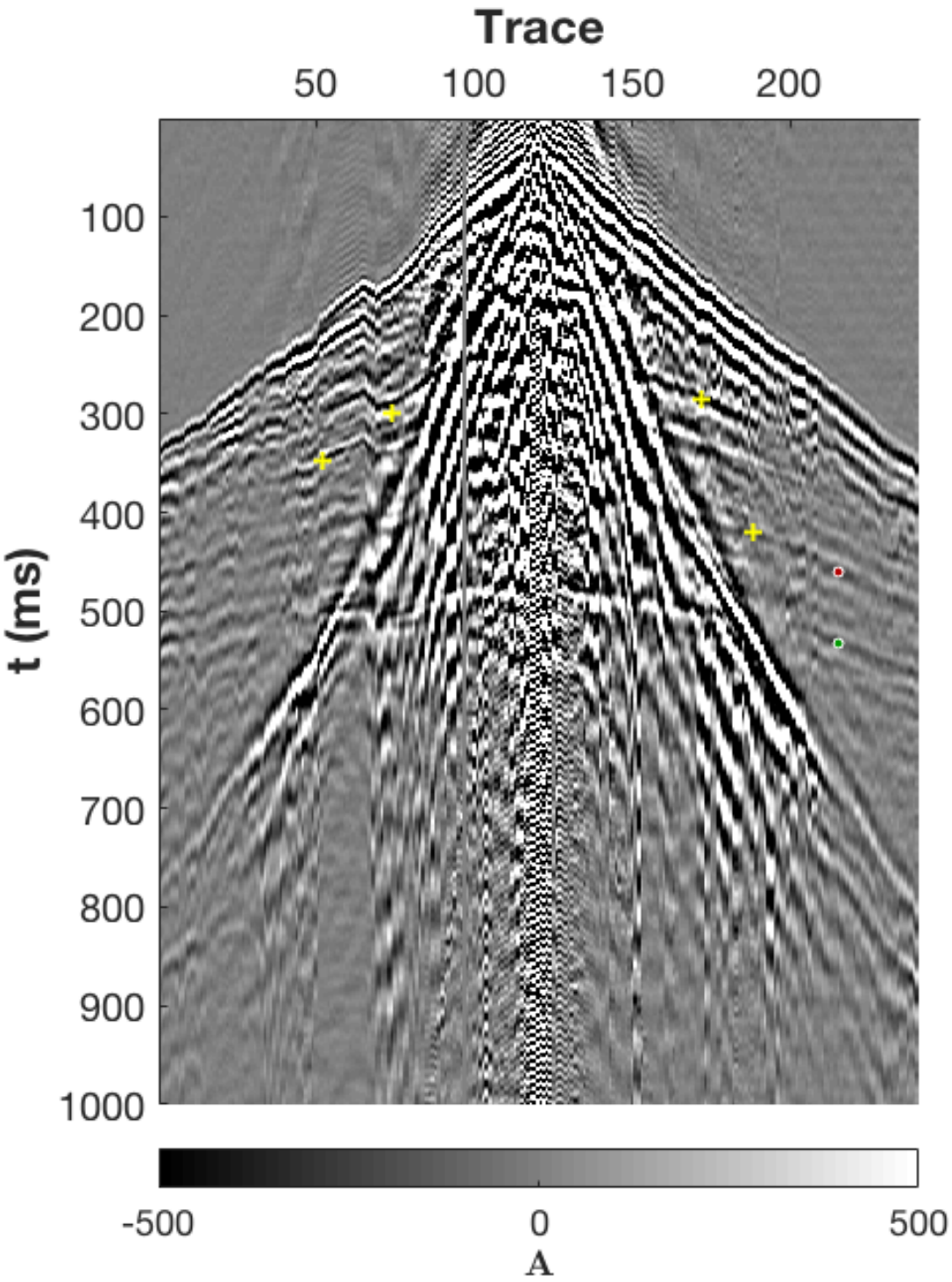


Figure 2.2: An example of a shot recording for 100 experiments. The red and green dots indicate points for which I analyze the reflection amplitude and position. The blue crosses indicate where I form amplitude distributions.

Data were acquired using split-spread acquisition, using a Vibroseis source, and 120 stations on either side of the siurce. The station spacing was 10 meters, and each station consists of a group of 6 geophones spread symmetrically around the station. The upper part of Figure 2.1 illustrates the setup. In order to test repeatability, one shot, 10 s long non-linear 4-128 Hz upsweep), was repeated 100 times within 1 hour. An example of a shot record for experiment A is shown on Figure 2.2.

Some of the 100 shot records are affected by noise from sporadic traffic. After sweep correlation, traffic noise is very strong and has spike-like character. Thus, affected samples appear as extreme outliers in data and bias the derived distributions. To mitigate the effect of traffic noise on uncertainty analysis, I apply a median filter along the experiment axis, as only some shots among the 100 experiments were affected by traffic noise. Figure 2.3 shows a receiver gather before and after filtering. Only median filtering is performed on data since my objective is to look at their uncertainty after as little processing as possible.

2.2.2 Experiment B: 10 shots repeated at 10 nearby locations

Experiment B was recorded on two acquisition systems: the wired system from experiment A and a wireless system. The two independent systems enable a direct comparison, with particular emphasis on the uncertainty of recorded data, short-term repeatability, data clarity and sensitivity to source position changes.

One dataset was recorded on the wired system using a similar setup to the experiment A, but with 115 geophones on either side of the source. The wireless nodes were installed to partially overlap with the wired system (Figure 2.4). The node spacing was 1.25m and every node recorded independently, whereas the wired system grouped the 6 channels to form one trace at each station. The 10 shooting locations were finely spaced at just a fraction of a wavelength, as illustrated in Figure 2.6. The 12 s long non-linear 4-140 Hz upsweep was repeated 10 times at each location. An example of a shot record from the wired and wireless systems is shown in Figures 2.5(a) and 2.5(b). For clarity, I use the label B_1 to refer to data recorded on the wired system and the label B_2 to refer to data recorded on the wireless

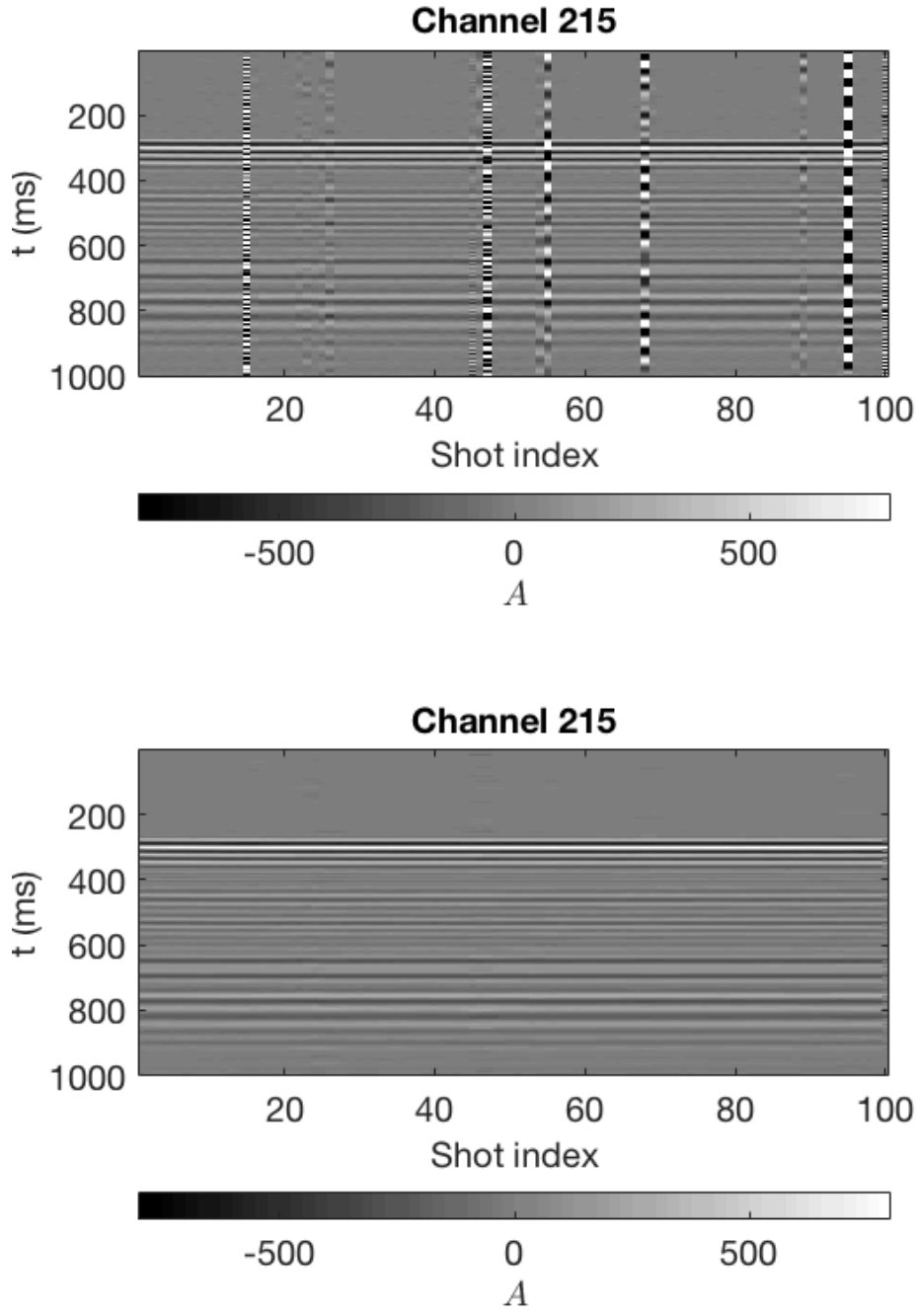


Figure 2.3: Receiver gather with car noise (top) and after median filtering along the experiment axis (bottom). Note that a large portion of noise is removed, but filtering residuals are present, e.g. for shot index 100.

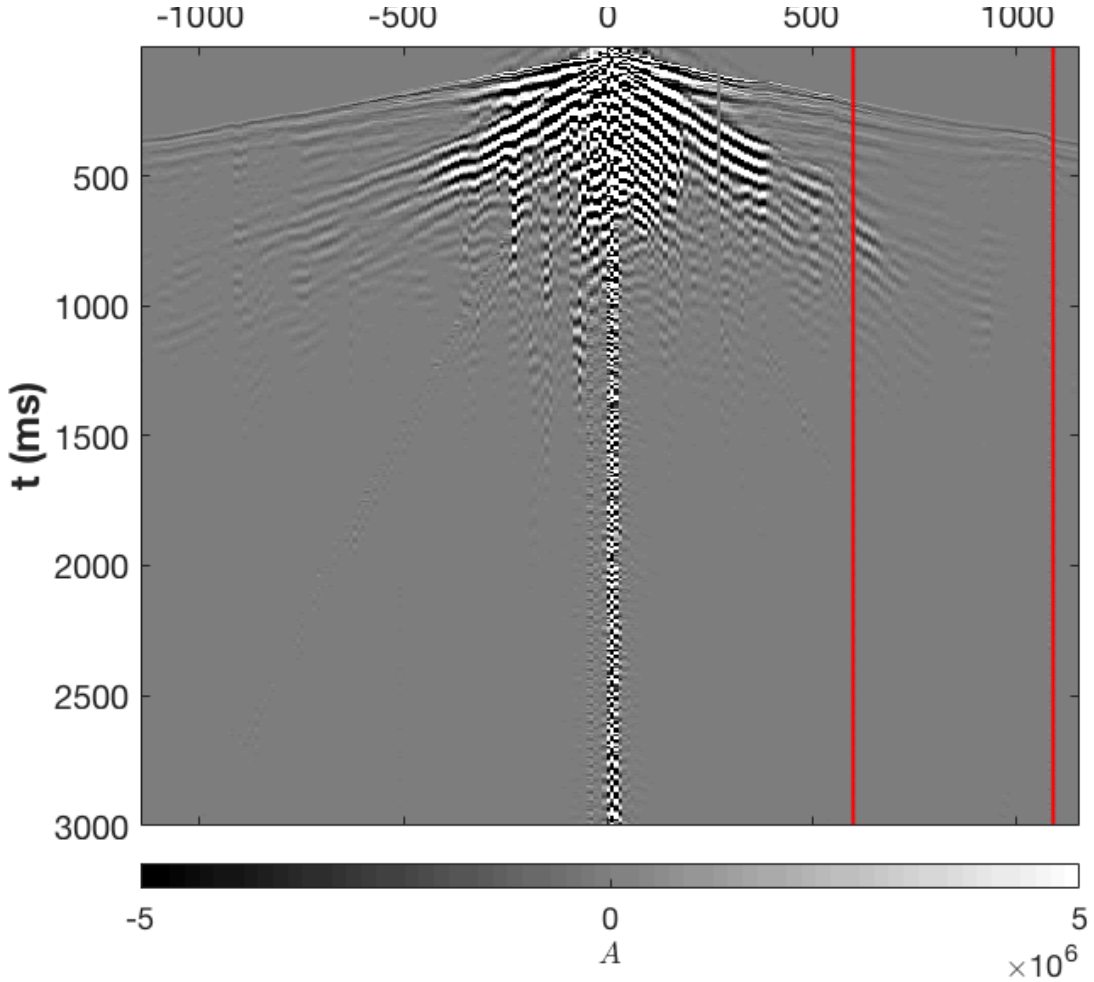
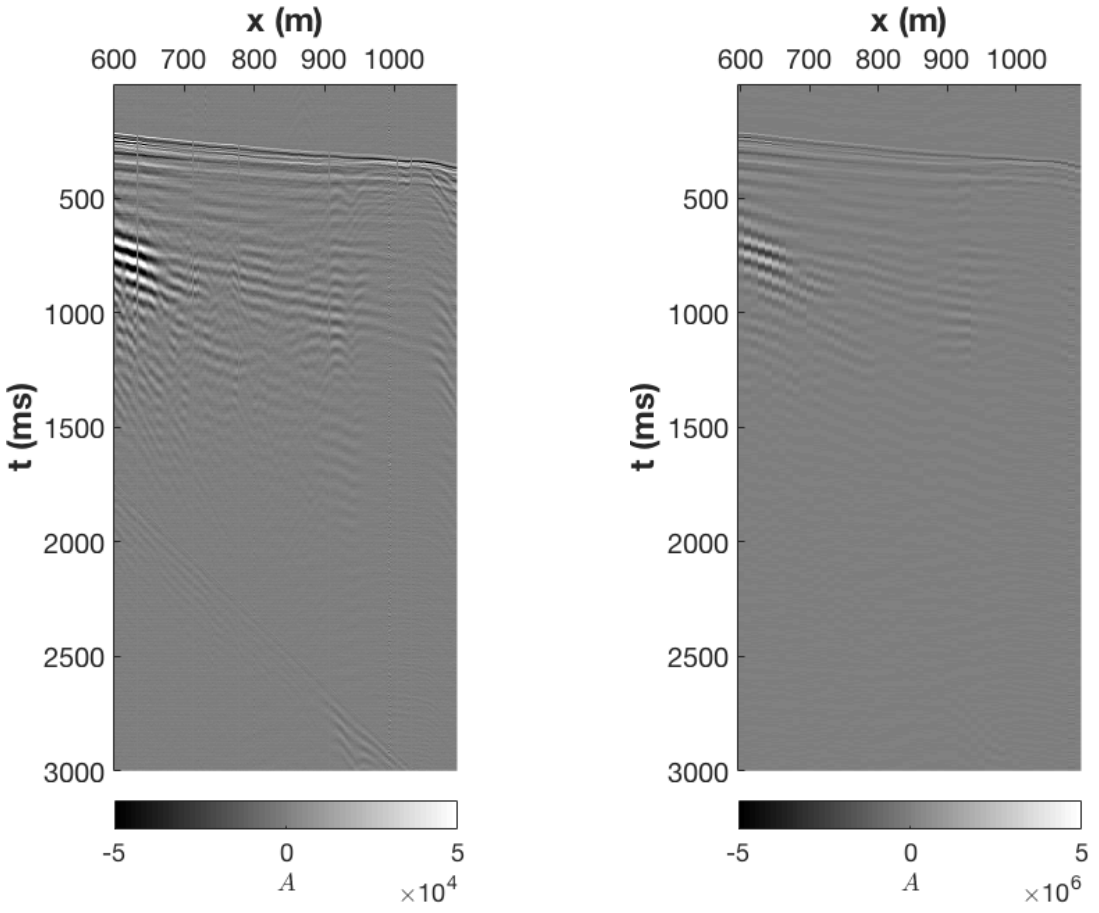


Figure 2.4: An example of data recorded on wired system for 10x10 experiment. The region between red lines indicates where wireless data are available. Note that reflection signal is not clearly visible on this raw shot record.



(a) (b)

Figure 2.5: (a) An example shot recorded on the wireless system and (b) the same shot recorded on the wired system. Note the difference in data readability, especially for the slow events.

system.

Similarly to experiment A, some records are affected by traffic noise. However, I only quantify the uncertainty of the first 10 shots, which were not affected by traffic noise. On the amplitude plots as a function of shot index (Figures 2.16 and 2.17), traffic noise has spiky character, but is easily identifiable and does not interfere with amplitude trends.

2.3 Methodology

I analyze the acquired seismic data with two main objectives: quantifying the uncertainty and assessing the short-term repeatability of reflection data.

To meet the first objective, I use an empirical PDF-based approach and a sample statistics approach. The PDF approach is appropriate for experiment A, as 100 samples for all times and positions are available to form empirical amplitude distributions. I describe data as a volume with dimensions t, x and e - time, offset, and shot index, where $N_e = 100$. At every (t, x) point, there are 100 amplitude values that I use to create a PDF $f(A(t, x))$. Given this PDF, its mean and variance can be computed at every t and x:

$$\bar{A}(t, x) = \sum_{A \in f(A)} A(t, x) f(A(t, x)) \Delta A, \tag{2.1}$$

$$\sigma^2(t, x) = \sum_{A \in f(A)} (A(t, x) - \bar{A}(t, x))^2 f(A(t, x)) \Delta A, \tag{2.2}$$

where $f(A(t, x))$ is the estimated PDF, ΔA is the amplitude bin size, and summing is for all amplitudes in the range of the PDF. The standard deviation σ is a proxy for the amplitude uncertainty. I assess the repeatability of reflections by tracking their time and amplitude on a high fidelity seismic trace with easily identifiable events. Trace fidelity F, which helps to identify reliable channels, is computed as a sum of standard deviations for all samples of the trace:

$$F(x) = \sum_{t} \sigma(t, x). \tag{2.3}$$

The typical repeatability metrics used in time lapse seismic, normalized RMS and predictability (Kragh and Christie, 2002) are not feasible for the experiment A since such



Figure 2.6: Marks on the road indicating the position of Vibroseis plate for experiment B. The distance between consecutive shot location is on the order of 1-2m.

measures are designed to track the changes between two surveys. Here, my objective is to quantify uncertainty, and not to compare individual shots (each shot pair would have their own NRMS or predictability). An alternative repeatability metric is standard deviation, but because it may depend on individual sensors' amplitude response, I propose to measure amplitude repeatability as the ratio of standard deviation to absolute mean amplitude:

$$R(t,x) = \frac{\sigma(t,x)}{|\bar{A}(t,x)|}100. \tag{2.4}$$

Perfect repeatability would correspond to $\sigma = 0$ and $R = 0$, which implies no amplitude uncertainty.

Data PDFs can be estimated if there are sufficient observations. In experiment B, the 10 amplitude samples per every shot location are not sufficient to estimate an empirical PDF. An alternative way of estimating uncertainty, that does not rely on known distribution and can be applied for any number of observation, is simple sample statistics. In this approach, the mean and variance are computed as:

$$\bar{A}(t,x) = \frac{1}{N_e}\sum_{i=1}^{N_e} A_i(t,x), \tag{2.5}$$

$$\sigma^2(t,x) = \frac{1}{N_e - 1}\sum_{i=1}^{Ne}(A_i(t,x) - \bar{A}(t,x))^2, \tag{2.6}$$

where $N_e = 10$ and i is the shot index.

To compare data acquired with the two acquisition systems, I compute the total repeatability of a shot at a given location as:

$$SR = \frac{1}{N_t \cdot N_x}\sum_{t,x} R(t,x), \tag{2.7}$$

where N_t is the number of time samples in a trace and N_x is the number of recorded traces.

2.4 Uncertainty quantification results

The uncertainty is described by mean and standard deviation maps, which I compute using the approaches described in the previous section. In experiment B, I only use the first 10 shots corresponding to the first source location, as these shots contain no traffic

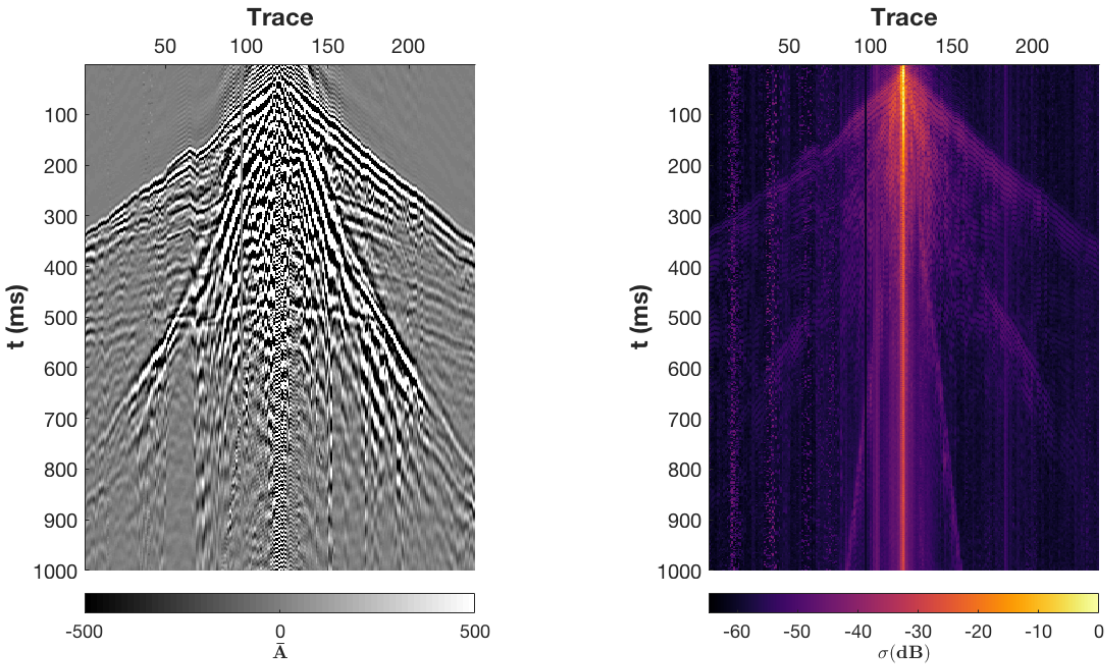
noise. Figure 2.7(a) shows the mean data amplitude for experiment A, computed with equation 2.1. Figures 2.8(a) and 2.9(a) show the mean data amplitude for experiments B_1 and B_2, respectively. Note that, compared to the raw data in Figure 2.5(a), the high frequency noise is attenuated (for example, in the first 200ms of recording). Similarly, in experiments A and B_1 the mean is a less noisy version of raw data. Most importantly, all seismic events excited by the seismic source are consistent, i.e. computing the mean does not appear to change the time and space positioning of these events.

The data mean representing the expected amplitude, allows one to compute the standard deviation representing the associated uncertainty. Since the energy present in seismic data decays rapidly with offset, seismic amplitudes have a wide range of values. The standard deviation associated with seismic amplitudes also has a wide range of values and for that reason, I show standard deviation maps (Figures 2.7(b), 2.8(b), and 2.9(b)) on the decibel scale.

The biggest uncertainty corresponds to the region directly under the seismic source, as depicted by Figure 2.7(b). In general, the data uncertainty decreases with increasing offset. Furthermore, waves traveling in the shallow parts of the subsurface (surface waves and head waves) and through the air have high uncertainty. In contrast, the data uncertainty related to reflections (which are easily identified for the experiment A) is small and does not stand out. Some patterns visible on the standard deviation maps are artifacts from imperfect traffic noise attenuation (e.g. trace 50 in Figure 2.7(b)), indicate dead traces (black lines in Figure 2.7(b)), or indicate consistently noisy channels (purple line in Figure 2.7(b) and yellow lines in 2.9(b) and 2.8(b)). The correlation between the seismic energy and uncertainty suggests that recording system characteristics, such as amplitude response and instrument gain, contribute to the data uncertainty.

The uncertainty levels for the two recording systems in experiment B are not the same: the standard deviation is higher for the experiment B_1. However, that fact alone does not imply that the wired system is less reliable. As explained before, the uncertainty is

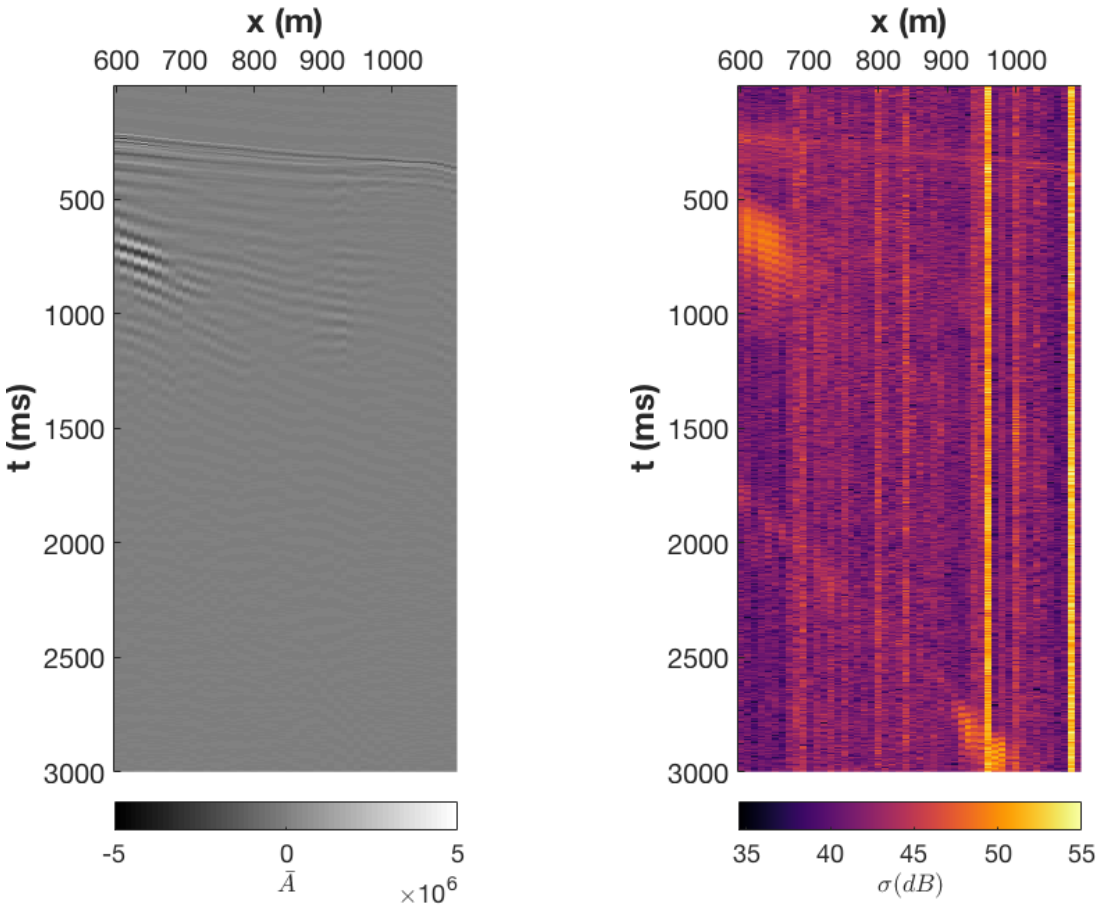
proportional to the amplitude, and all data amplitudes recorded on the wired system are about two orders of magnitude higher than those on wireless system. This difference in amplitude is caused by different amplitude responses and gains in the two systems, which does not allow direct comparison of the amplitudes or uncertainties. The systems can be compared by looking at the repeatability R, which I discuss in the next subsection.



(a) (b)

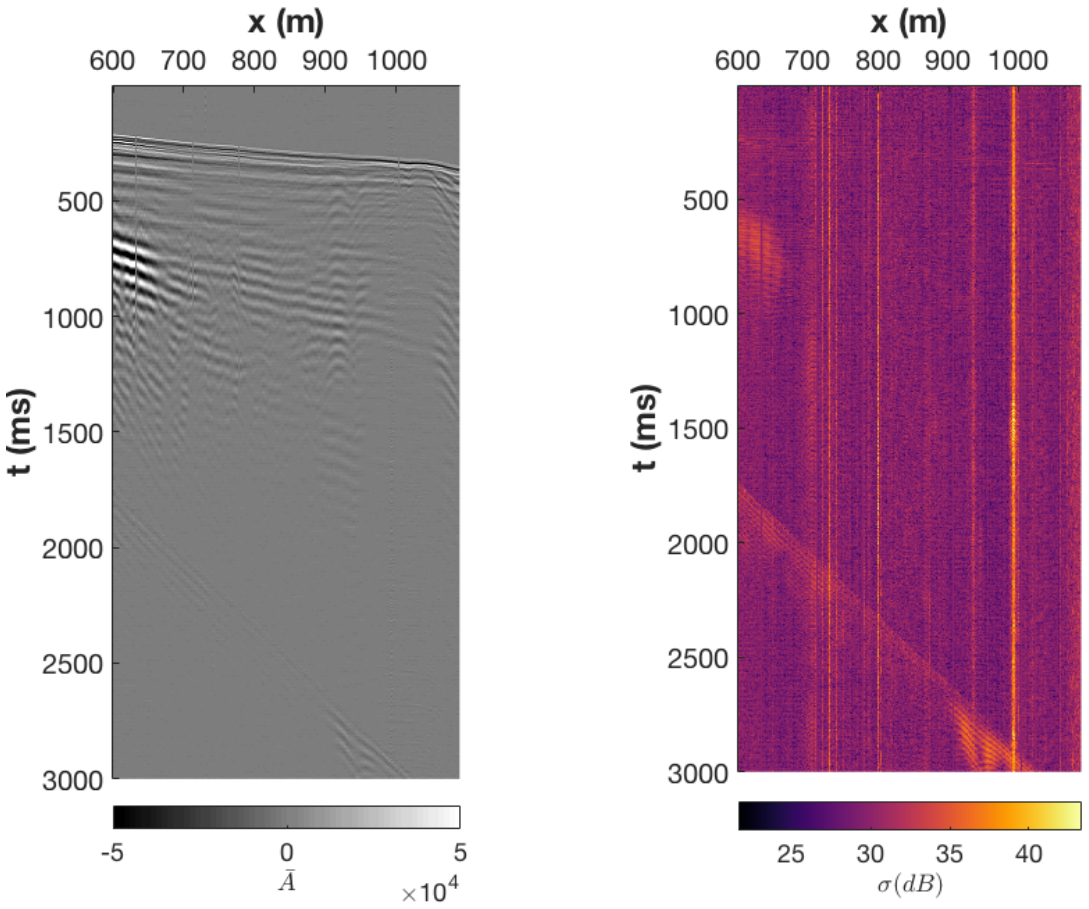
Figure 2.7: (a) The mean amplitude and (b) the standard deviation for experiment A, computed using equations 2.1 and 2.2.

As explained before, one of the objectives for the data analysis in experiment A is to verify whether the amplitude distributions for seismic events, especially reflections, are Gaussian. I consider four points, indicated by blue crosses in Figure 2.2, to analyze reflection amplitude distributions. Figure 2.10 shows the distributions derived from median-filtered data for experiment A. I form the distributions from data histograms at a given time and position. Note that the amplitude range is different for the different points, but the bin size is constant.



(a) (b)

Figure 2.8: (a) The mean amplitude and (b) the standard deviation for 10 shots recorded on the wired system.



(a) (b)

Figure 2.9: (a) The mean amplitude and (b) the standard deviation for 10 shots recorded on the wireless system.

The distributions are not Gaussian, especially in Figures 2.10(c) and 2.10(d) - the latter is clearly bimodal. Thus, I conclude that that data noise, when observed within one hour, is not of Gaussian character. More observations over a longer period of time could paint a different picture, as noise levels vary, depending on the time of the day, weather conditions and other environmental factors.

The non-Gaussian character of data distributions has important implication for solving inverse problems. The data prior should be an accurate representation of the observed reality, so that the solution is reliable. Gaussian distributions, though convenient to use, do not capture real observations well. It is especially important for solving the inverse problems which heavily rely on accurate amplitude information, such as FWI. Having the right idea about data distribution helps to constrain the answer.

2.5 Data repeatability

The analysis of short-term repeatability provides insight into seismic data noise levels (changes in elastic moduli of a medium are not expected except the immediate vicinity of the seismic source) and can be used to compare two acquisition systems. Therefore, I assess data repeatability for experiments A and B, but with slightly different focus for each.

The goal of experiment A is to assess short-term seismic acquisition repeatability. I approach this problem by analyzing the recorded traveltime and amplitude on a reliable trace with a good reflection signal. The red and green dots on Figure 2.2 indicate the reflections of interest. Figure 2.12 shows the raw trace, its mean and its standard deviation as a function of time. Note that the largest uncertainty corresponds to the strongest events (in this case surface waves), which can be explained either by the instrumentation gain or small changes in the shallow subsurface through which these waves propagate. For all shot indices, I track the events marked by the red and green dots. The kinematics of the reflections, shown on Figure 2.13, are highly consistent, differing only by a maximum of 3ms for the shallower event and 1ms for the deeper event. The reflection amplitudes, also shown on Figure 2.13, are not as consistent; one may observe fluctuations that are visibly

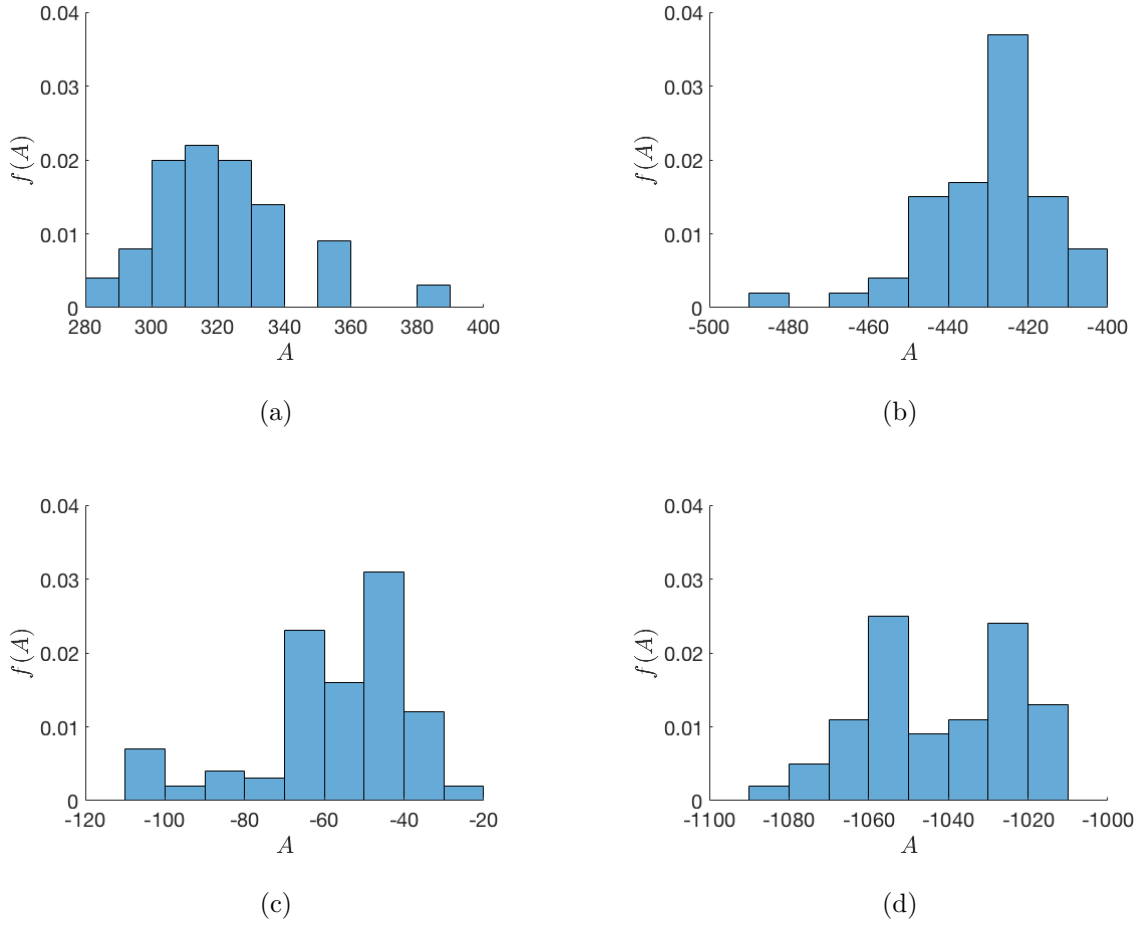


Figure 2.10: PDF's for data points indicated by blue crosses on Figure 2.2. Distribution shapes are not Gaussians.

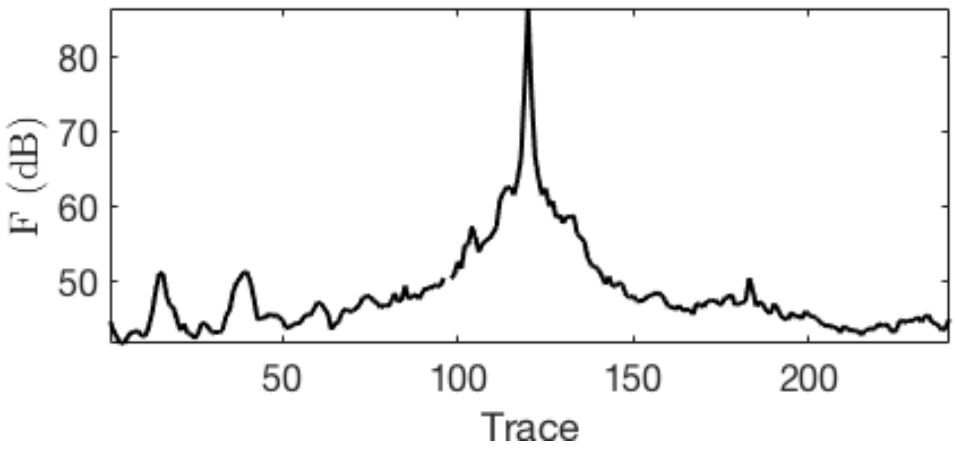


Figure 2.11: Trace fidelity computed using equation 2.3. Channel reliability increases with offset.

correlated for the two events. Some of the fluctuations can be explained by the imperfect removal of traffic noise (e.g. large amplitude decrease for shot 53). If several consecutive shots contain car noise, then the median filter needs larger window (I use 5 samples long) to remove that noise from data. However, a larger window would also smooth the noise not related to traffic, which is not desirable since that is the noise I aim to characterize. An alternative way of dealing with traffic noise, potentially more efficient, is to treat noise removal as a source separation problem, and use the existing techniques, such as independent component analysis, on uncorrelated shot records (Lee, 1998). Aside from the small traffic noise remanent, the changing reflection amplitudes are due to uncontrollable environmental conditions. The solid black line indicates the mean amplitude, while the dashed lines mark $\pm$ one standard deviation. The repeatability R, as defined in equation 2.4, is 5.4% for the shallower event and 4% for the deeper event. Therefore, amplitude changes not related to elastic moduli changes are small, and should not interfere with detectability of time lapse signals. Furthermore, short-term repeatability can be improved for example by burying the recording array or placing it in boreholes, thus isolating some of the environmental factors

affecting repeatability. Repeatability feeds into subsequent processing, e.g. through imposing constraints or guiding search of regularization term in FWI.

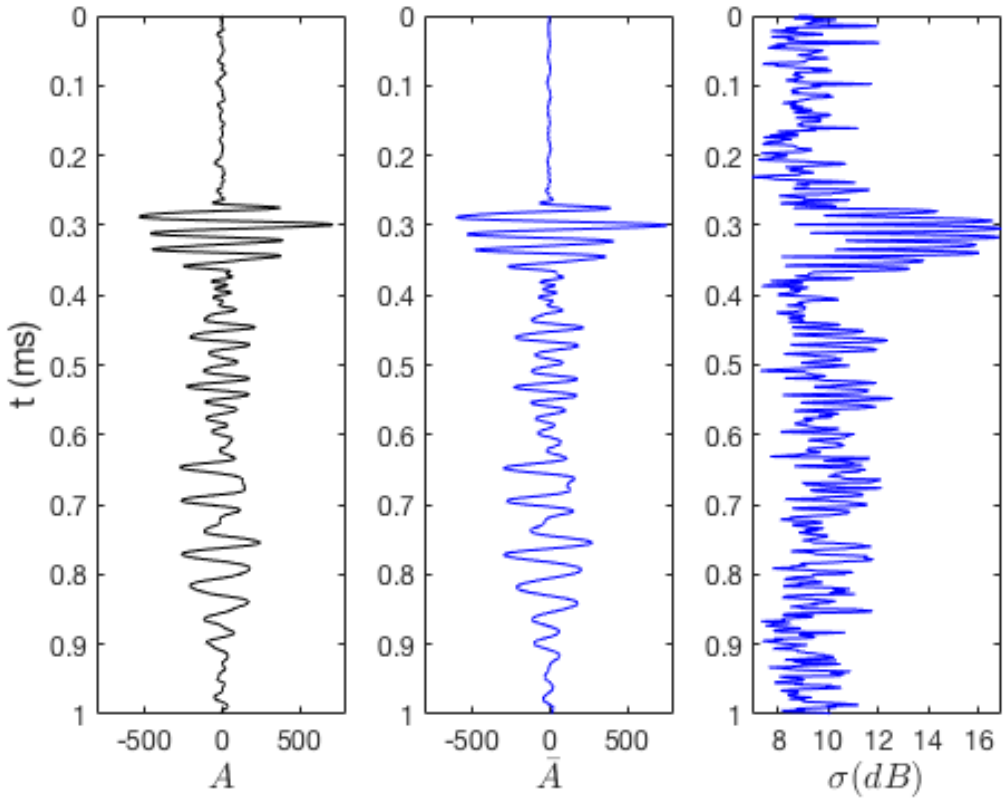


Figure 2.12: From left to right: a trace 215 extracted from shot 2 (experiment A), its mean and standard deviation as functions of time.

The repeatability study for experiment B provides insight into short-term repeatability of seismic data and enables a comparison between two recording systems. If a seismic event is highly repeatable, R is small. The second objective of this repeatability study is to examine the sensitivity of seismic amplitudes to small changes in the source position.

Figures 2.14 and 2.15 depict the data repeatability for experiments B_1 and B_2, respectively. The first panel on both figures shows the full, not clipped range of repeatability values. The repeatability range is wider for experiment B_2, which is expected since the

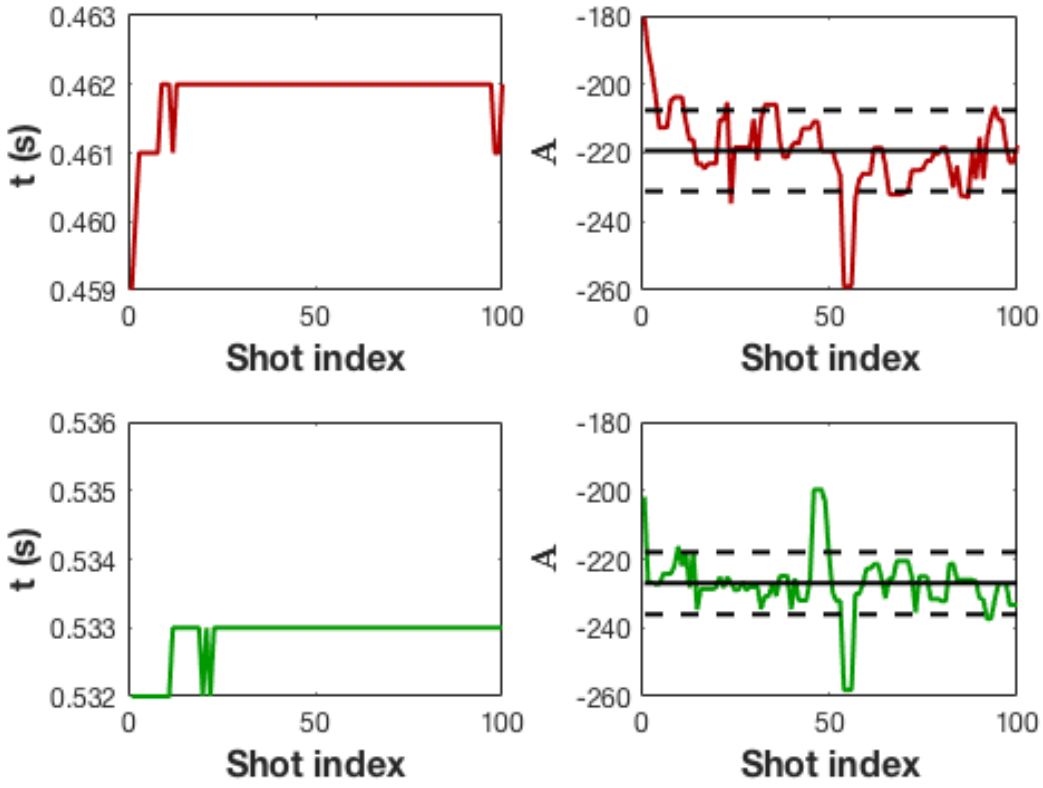


Figure 2.13: Reflection time uncertainty (left) and amplitude uncertainty (right) for events indicated on Figure 2.2. The kinematic repeatability is high, while the amplitude fluctuates.

wireless system does not have any averaging mechanism built-in, unlike the wired system that averages inputs from 6 geophones in a group. In the middle panel of Figures 2.14 and 2.15, R is clipped to values below 0dB, that is, events for which amplitude variation between first 10 shots is less than 100%. As expected, coherent seismic events are highly repeatable. One may observe that regions of particularly high repeatability are consistent between experiments B_1 and B_2. For example, the headwave around $x = 1000$m in the middle panels of Figures 2.14 and 2.15 is highly repeatable. High repeatability is important for time-lapse monitoring. If the repeatability is poor, one cannot distinguish between amplitude changes due to changes in the medium and the amplitude changes caused by noise. The third panel of Figures 2.14 and 2.15 shows data with repeatability between 0 and 3dB. The black color corresponds to highly repeatable events, while lighter colors represent non-repeatable signal. Figure 2.15 is easier to interpret, with black seismic events and a background which looks like white noise. Figure 2.14 also have clear seismic events, but the background character is not clear. Furthermore, some of the slow events in experiment B_1 are spatially aliased, challenging interpretation. The comparison of Figures 2.14 and 2.15 reveals that repeatability of the wireless system is good despite recording individual trace, instead the averaging the multiple inputs like the wired system. The biggest repeatability difference is for the signal not excited by the seismic source. Note that the range of repeatability is bigger for the nodal system, that is, it records highly non-repeatable events. This is because some of the ambient noise, visible on a seismic trace for example just before the first breaks, is attenuated by the wired system through averaging. To attenuate some of the ambient noise in wireless system, one can use the same averaging procedures that are inherent in the wired system after data are acquired. However, after performing some filtering (e.g. simple low-pass filter), one may also keep the finely spaced traces to improve the data interpretation. Notice that spatial aliasing on a wired system prevents the correct interpretation of slow events (e.g. compare the third panels on Figures 2.14 and 2.15). Therefore, the wireless system gives more acquisition and processing flexibility.

In the study of time-lapse seismic changes, repeating the acquisition geometry accurately is important, since the distance from the source directly affects the recorded amplitude. One would like to interpret changes in amplitudes related to medium properties, not to inaccurate geometry. In the following, I study the sensitivity of the land seismic data to small source position changes (a fraction of the wavelength). Similar source mispositioning may naturally occur, for example, from inaccurate coordinates. To study the effect of source position on the amplitudes on seismic data, I select two locations in time and space to examine the amplitude as a function of shot index (Figures 2.16 and 2.17). The data amplitudes recorded on both systems reveal distinct, stair-like pattern, that matches exactly the source position changes after every 10 shots. In Figure 2.16, amplitude for experiment B_1 decreases for the first 60 shots and increases afterwards. The amplitude for experiment B_2 decreases steadily for all shots. The amplitude behavior in Figure 2.17 is consistent for both systems, except for the spike of traffic noise at shot 60, that is only picked up on the wired system, due to group averaging. Significant amplitude changes due to the source location highlight the importance of geometry repeatability for time-lapse studies.

2.6 Discussion and conclusions

My analysis shows that data uncertainty is variable and depends on time and position. The most uncertain data region is directly below the seismic source. This is related to the experimental conditions, since the coupling between the shaker's plate and the dirt road changes as the ground compacts. It is an unavoidable pitfall of repeated experiments in the field: elastic properties in close vicinity of the source change as the source is activated over time. The biggest amplitude change, likely caused by compaction, can be observed at the beginning of the experiments (Figure 2.13). However, such changes have a minor effect on data as the offset increases.

High energy events, such as surface waves and head waves, also have high uncertainty. Traveling in the shallow subsurface, they are the most affected by environmental factors. Assuming no changes to the medium, the traveltimes do not change. However, the amplitudes

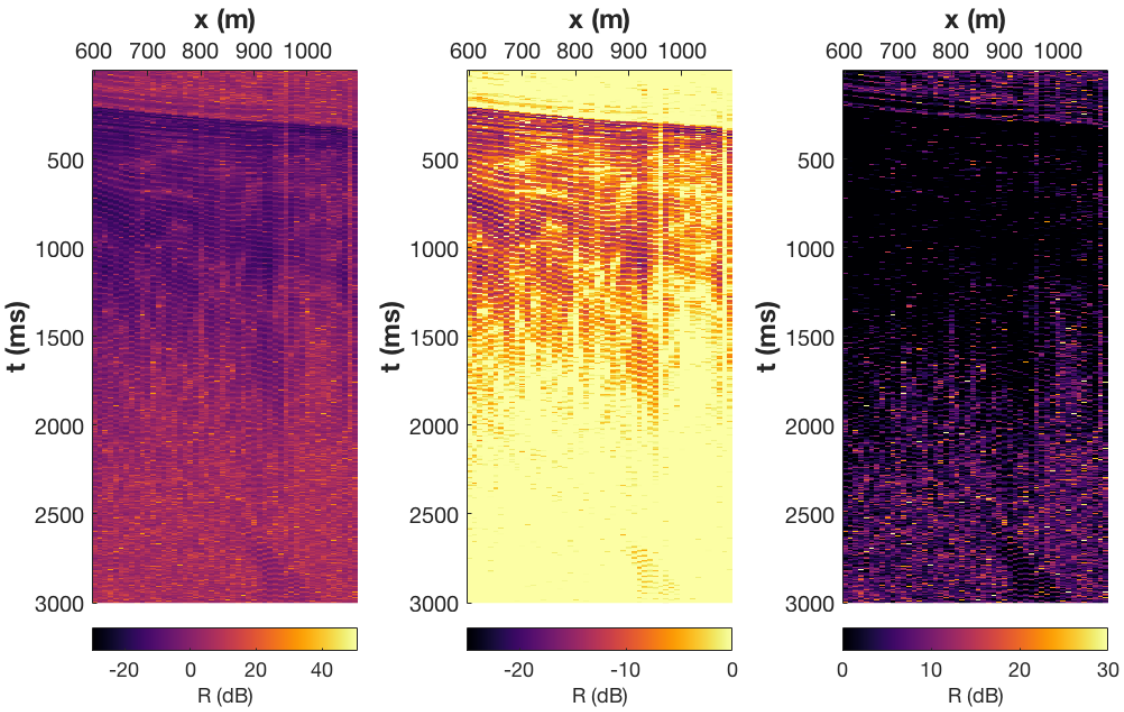


Figure 2.14: Different ranges of repeatability index for experiment B_1. Seismic events excited by the source are highly repeatable, but some of them are aliased.

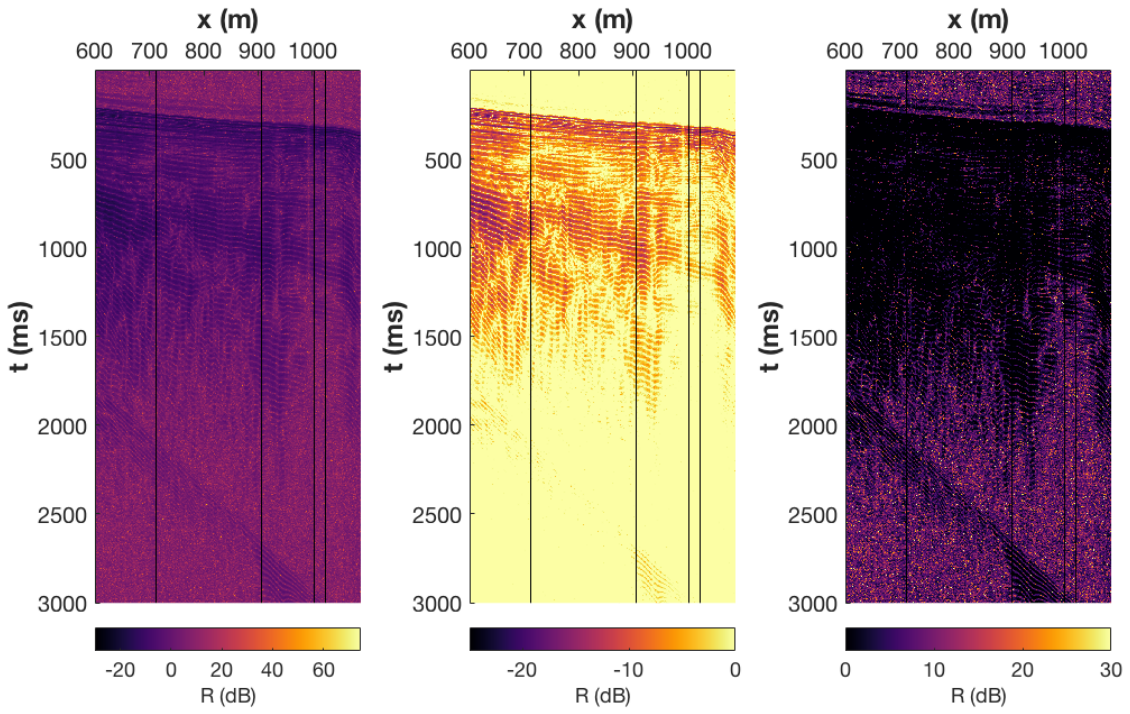


Figure 2.15: Different ranges of repeatability index for B_2. Dark lines indicate dead channels. Seismic events are highly repeatable and non-aliased.

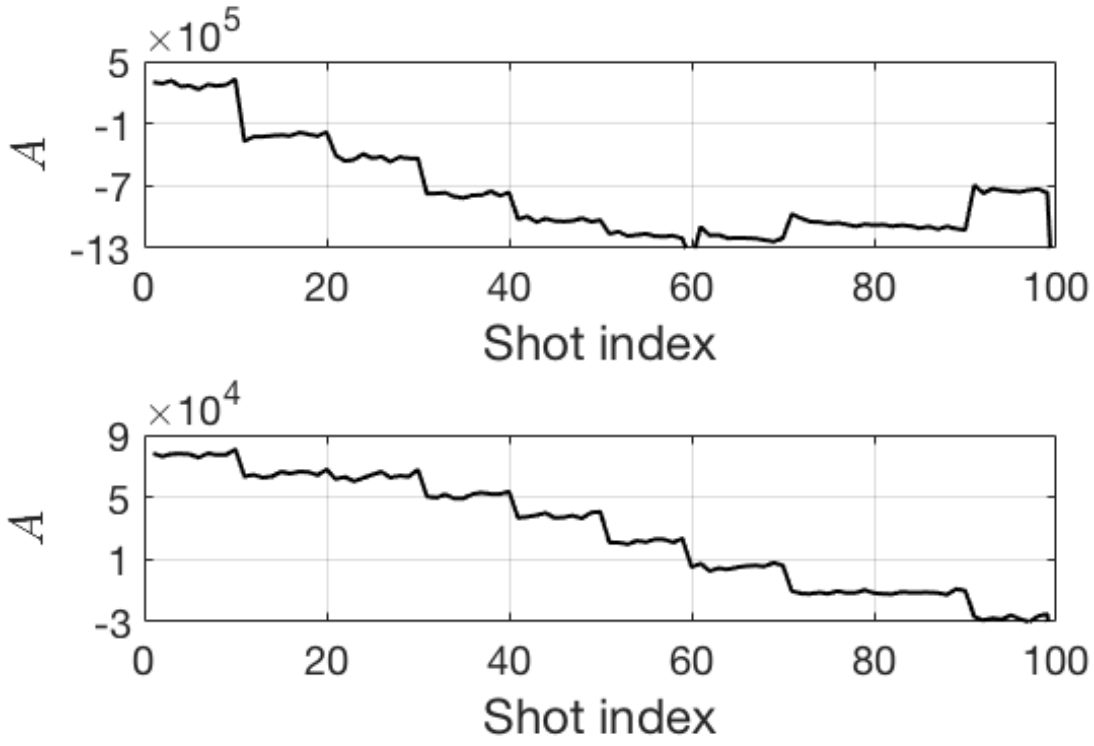


Figure 2.16: Comparison of amplitude as a function of shot index for $t = 770$ms, $x = 620$m for experiment B_1 (top) and B_2 (bottom). The stair-like pattern is reflecting changes in the source location, but the behavior of the amplitude for the two systems is not consistent after the shot 60.

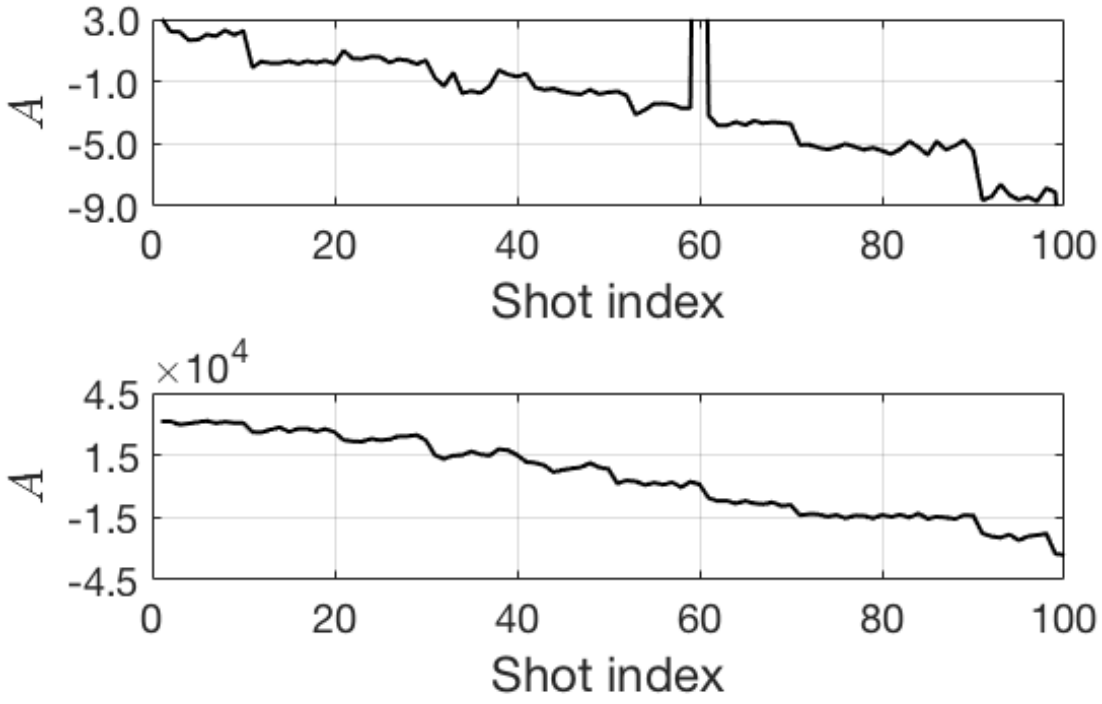


Figure 2.17: Comparison of amplitude as a function of shot index for $t = 243$ms, $x = 680$m for experiment B_1 (top) and B_2 (bottom). The stair-like pattern is reflecting changes in the source location and the behavior of the amplitude for the two systems is consistent except for the spike of noise for shot 60.

can change because of noise, which may cause an apparent shift in observed traveltimes, as is the case for the reflection traveltime shown on Figure 2.13. Due to the short experiment duration, the noise causing amplitude distortion is not related to temperature changes or soil saturation. The uncertainty is approximately proportional to the magnitude of a seismic event. Therefore, the noise is not a simple random variable with fixed standard deviation and should not be modeled as such. I interpret that uncertainty is mostly related to the sensors noise, as it is correlated with the mean amplitude.

Seismic reflections, whose energy is orders of magnitude smaller than the energy of the surface waves, also have much smaller uncertainty. The kinematics of reflections are highly repeatable, while amplitudes fluctuate, albeit consistently. Therefore, inversions that use the amplitude information are more uncertain than those relying on traveltimes only. For seismic imaging, the reflector positioning is more certain than the image amplitude, assuming that only data, and are uncertain. Furthermore, high repeatability and small reflection uncertainty implies that changes observed in time-lapse signals can be attributed to the physical changes in the medium with high probability.

My analysis shows that seismic data distributions are not Gaussian. Nor are they consistent for different (t, x) samples (Figure 2.10). The question that springs to mind is: how would using the true distributions affect the results of inversion? Data prior is often treated as a normalization constant in the Bayesian framework (Ely et al., 2018). Incorporating the information about uncertainty may improve posterior estimates by introducing realistic data constraints. Furthermore, since the distributions are not Gaussian, the well known formula for the maximum a posteriori model (discussed in Chapter 1) does not apply (recall that in its derivation, all distributions are assumed to be Gaussian). In the deterministic framework, the uncertainty information can be used to determine the optimal data misfit, or to pick data regularization term.

The data repeatability plots (Figures 2.14 and 2.15) give the basis for comparison between the wireless and the wired recording systems. Both systems have different amplitude

responses and as such, the amplitudes registered on them are not directly comparable. The uncertainty, captured by the standard deviation, is proportional to the amplitude, leading to order of magnitude differences in uncertainty for the same types of waves. Thus, according to standard deviation alone, the wired system has higher uncertainty than the wireless system, simply because the recorded amplitudes are up to two orders of magnitude higher than for the wireless system. However, one can compare the two systems on grounds of data repeatability. The seismic signal generated by the source has similar repeatability levels, as depicted in Figures 2.14 and 2.15. The total repeatability of a shot (SR) is 47.1 for the wireless and 11.1 for the wired system. The spatial averaging between the channels in a geophone group helps with the noise attenuation, thus the total repeatability of a wired system is higher. Despite this advantage of a wired system, a very fine spatial sampling possible with the wireless system can greatly improve the understanding of wave phenomena propagating at slow velocities (e.g. non-aliased surface waves) and help one distinguish between noise and signal with greater accuracy.

Amplitude changes due to slight source location changes are not straightforward to interpret. Ideally, the amplitude changes for a specific reflection should be examined. However, without some data processing to remove the high-energy surface waves, finding a reflection signal in raw data is challenging for experiment B (Figure 2.4). Thus, instead of using the reflection signal, I examine the imprint of source location changes on surface wave signal (Figure 2.16) and head wave signal (Figure 2.17).

The amplitude of a surface wave (Figure 2.16) shows clear, staircase-like pattern, that is correlated with changes in seismic source location. On the wireless system, the amplitude decreases as a function of source location and changes from high positive to negative. The wired system registers amplitude decrease followed by increase, while maintaining the staircase pattern. Headwave amplitudes decrease on both systems (Figure 2.17), but more smoothly on the wireless system. There are several things to consider to explain these observations. First, the source controller is directly connected to the wired system whereas

the nodes rely on shot GPS time stamps to extract data from continuous recording. A time stamp error could cause a slight time shift for the wireless system data. Second, spatial averaging builtin to the wired system affects slow events, such as surface waves, to a greater extent than fast events, like head waves or reflections. Third, changing the source location affects both the traveltime (signal would be registered earlier for a closer source position) and the amplitude (shortest distance implies smaller attenuation, thus larger amplitude). Fourth, the topography may influence the registered traveltimes at different receivers. Judging by the amplitude plots alone, it is impossible to explain which effects came into play and to what degree.

An important finding for the time lapse land monitoring is that seismic amplitudes are very sensitive to source location changes. However, from the exploration point of view, both surface waves and head waves are removed in processing. A similar sensitivity analysis should be performed on identifiable reflections, as their amplitude changes are of interest in 4D seismic monitoring.

CHAPTER 3

THE IMPACT OF VELOCITY UNCERTAINTY ON THE QUALITY OF THE SEISMIC IMAGE

Reliable uncertainty quantification in seismic imaging is still a major challenge due to many uncertainty sources that are difficult to account for: data noise, acquisition mispositioning, velocity and anisotropy uncertainty, source signature uncertainty, etc. The velocity model and anisotropy models, are major contributors to image uncertainty, since they affect the kinematics of wave propagation and thus, image focusing and reflector positioning.

To study the effect of velocity uncertainty on a seismic images, I introduce two subsalt microseismic imaging scenarios. Each scenario captures the geological uncertainty related to the salt body. I use the microseismic sources to illustrate simple and complex imaging scenarios by the source placement under sediments and under the salt and quantify image uncertainty in the Bayesian framework. The main outcomes of this analysis are image uncertainty maps described either as distributions of amplitude at every image location or as distributions of interpreted source locations. The amplitude distributions for the subsalt source are two times broader than for the subsediment source, indicating higher uncertainty. The image pixel uncertainty is best communicated in the form of confidence index maps, obtained by a linear transform of standard deviation maps. The source location PDFs reveal the uncertainty direction, but are strongly affected by the acquisition geometry.

3.1 Introduction

Seismic images provide a plethora of information about subsurface, such as the outline of geological structures or potential hydrocarbon accumulations. Once a feature of interest is interpreted on a seismic image, that interpretation is the basis for subsequent decisions. However, there are two main sources of uncertainty associated with interpreted features. First, the seismic image itself is uncertain due to many uncertainty sources, including data

uncertainty and velocity uncertainty (Osypov et al., 2008, 2013; Rawlinson et al., 2014; Yilmaz, 2017; Ely et al., 2018). Second, the same seismic image may be interpreted in many different ways by different interpreters, giving rise to interpretation uncertainty (Avseth et al., 2010; Freeman et al., 2010; Rapstine et al., 2016; Irakarama et al., 2017). In this chapter, I focus on the former type of uncertainty, while acknowledging that interpreter bias also has a role to play.

Several factors contribute to image uncertainty. Thore et al. (2002) discuss the effect of processing and interpretation steps on the uncertainty of the structural model and conclude that migration, horizon picking, and time-to-depth conversion usually have the largest impact. The common denominator for these uncertainty sources is the Earth model. The velocity and the anisotropy affect the kinematics of wave propagation and thus reflector positioning and the focusing of seismic events in a migrated image.

Information about velocity is derived from seismic data, sometimes also aided by well logs. Over the years, the velocity estimation techniques evolved, and with them, velocity uncertainty quantification. Early on, velocity estimation was based on a simple layered earth model assumption. Hajnal and Sereda (1981) quantify interval velocities uncertainty for layered earth models derived using the Dix formula (Dix, 1955). More recently, Buland et al. (2011) use the Bayesian framework to estimate Dix interval velocity and associated uncertainty. A more sophisticated approach to velocity estimation - tomographic traveltime inversion (Bishop et al., 1985) - does not assume layering and, on an intuitive level, should provide more accurate representation of velocity in complex geology regions. However, the tomographic problem is highly non-linear and gaining insight into velocity uncertainty is challenging. Osypov et al. (2013) use Bayesian inference to the linearized tomographic traveltime inversion and explore the nullspace of the tomographic operator by performing partial eigen-decomposition of the posterior model covariance. They also look at the impact of velocity on the image by performing map migration on a horizon of interest with different realizations of the velocity model. Landa et al. (1991) develop an alternative to ray to-

mography: coherency inversion with layer stripping, which they use to quantify the velocity uncertainty in velocities and of layer depths.

Unlike for the simple case of layered earth, where an analytical formula is available, quantifying uncertainty for complex, non-linear problem with complex models requires a probabilistic framework. A natural choice is Bayesian inference (Tarantola, 2005), since it allows to account for different sources of uncertainty. Within the Bayesian framework, one can incorporate data and model uncertainty as prior knowledge, and combine this information with theory and its associated uncertainty to obtain the posterior model distribution. The Bayesian framework is used to estimate the uncertainty of high-end model estimation techniques like full waveform inversion (FWI) by Fang et al. (2014), Zhu et al. (2016) and Biswas and Sen (2017). Ely et al. (2018) examine velocity uncertainty as well as image uncertainty by utilizing fast forward modeling and Metropolis-Hastings sampler to draw from the posterior distribution. They use such models to perform map migration on the horizon of interest and quantify the uncertainty of its position. Their workflow assumes that the velocity model is simple and can be described by few parameters. This assumption helps to significantly reduce the size of the problem of velocity estimation, but fails for models of greater complexity (e.g. with sharp interfaces such as sediments - salt boundary).

Salt bodies present a significant challenge to seismic imaging due to the sharp impedance contrasts, preventing energy from transmitting below the salt body, and due to the complex salt shapes distorting the shape of seismic wavefronts. At the same time, salt bodies are good traps for hydrocarbons, thus delineating their shape and finding what lies below the salt is of great interest in exploration.

The effect of incorrect velocity on images is known and can be recognized by characteristic frown or smile pattern, seen on overmigrated or undermigrated images, though these patterns become more complicated in complex velocity (Figures 3.2 and 3.3). However, the effect of local changes in velocity for complex models containing salt is not well studied. In this chapter, I examine the impact of uncertain salt velocity on microseismic source imaging. I

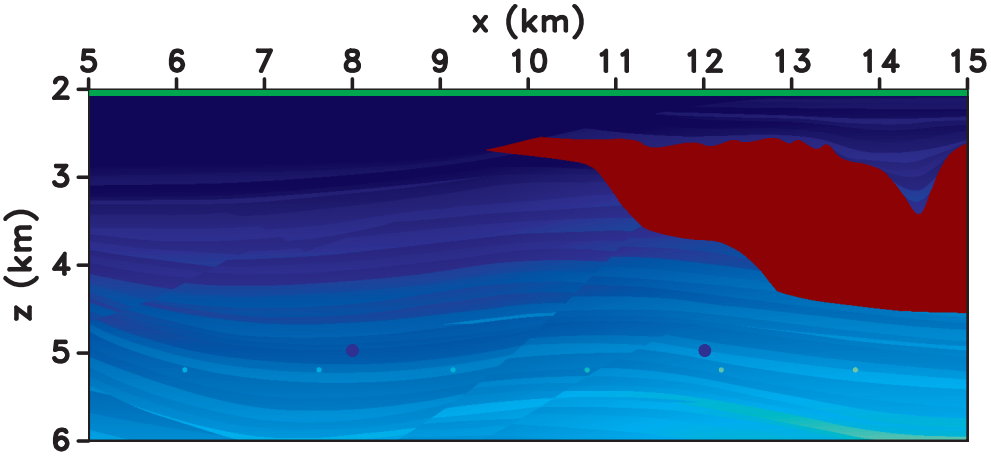
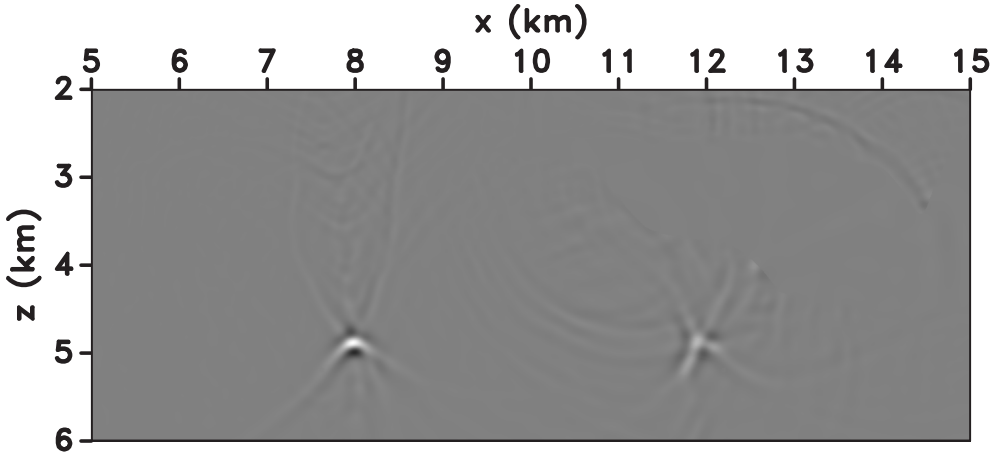


Figure 3.1: Velocity model with two scatterers, used to demonstrate the effects of too slow and too fast velocity on image focusing (Figures 3.2 and 3.3).

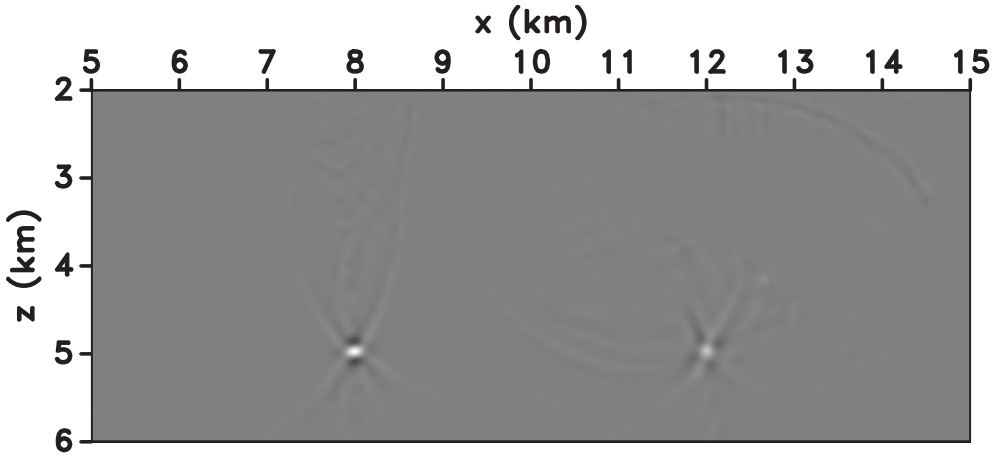
use this setup as a prototype for more complex subsalt imaging.

In the context of Bayesian framework, the velocity uncertainty is incorporated in the theory uncertainty. One way to quantify image uncertainty is to draw samples from the posterior distribution. Assuming that there are enough velocity model realizations to fully describe the range of velocity uncertainty for each scenario, the posterior images formed with uncertain models are an accurate representation of the posterior distribution.

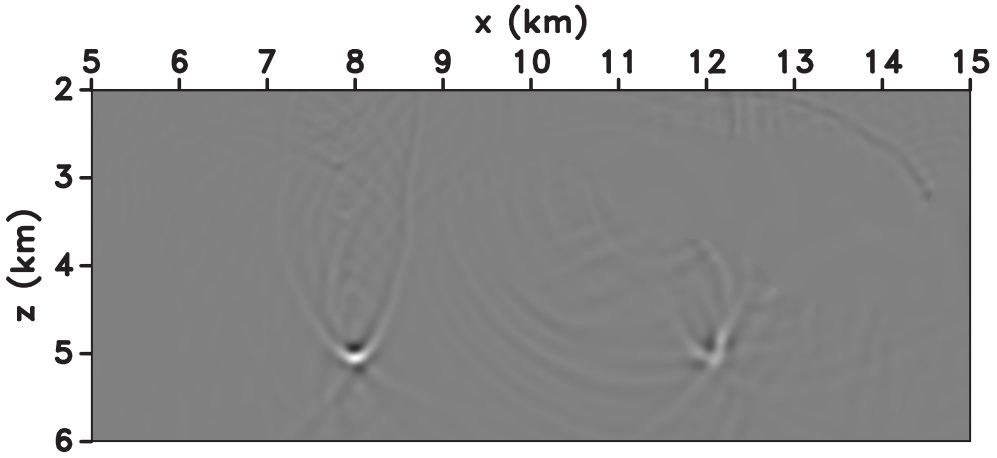
As indicated earlier, my study of image uncertainty is based on two geologically plausible scenarios containing features that are below the typical resolving power of seismic data (Jannane et al., 1989). In both scenarios, I analyze two microseismic sources: one under the sediments and one under the salt. These two targets are meant to represent imaging in simple and complex geological scenarios. The first scenario assumes that the salt bodies are not homogeneous and may contain inclusions of sediments, but the number, shape and placement of these sediments inside the salt is unknown. I generate 1001 velocity models with randomly placed inclusions on the order of the dominant seismic wavelength. One such model is chosen to represent the true structure and to generate data. The remaining 1000 velocity models are realizations representing theory uncertainty for the imaging problem, and I use them to form the posterior image distribution. The second scenario is motivated



(a)

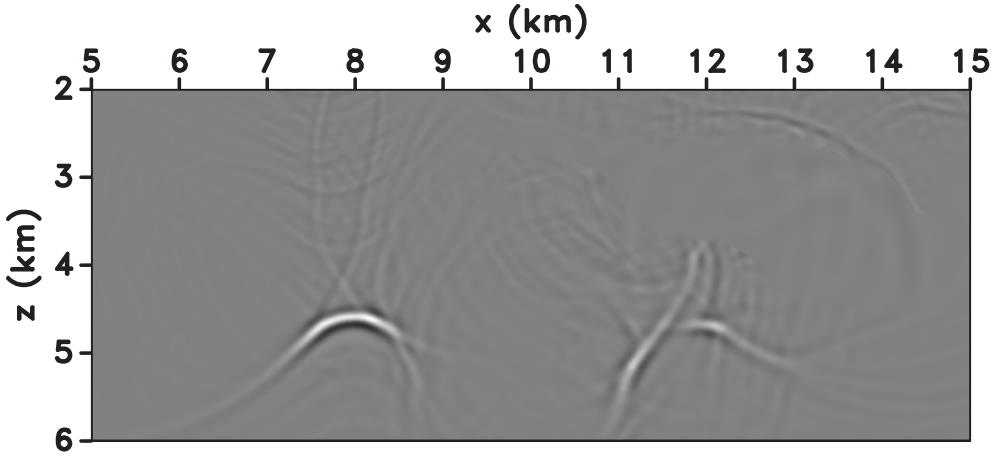


(b)

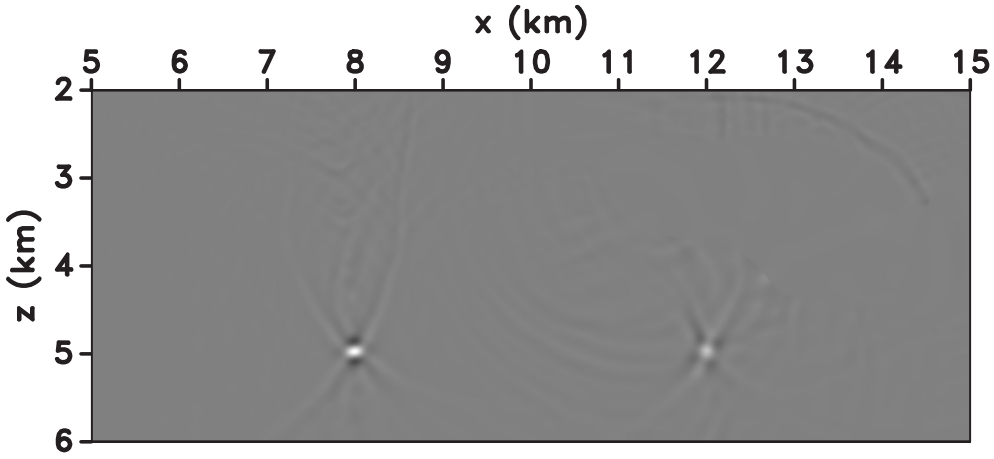


(c)

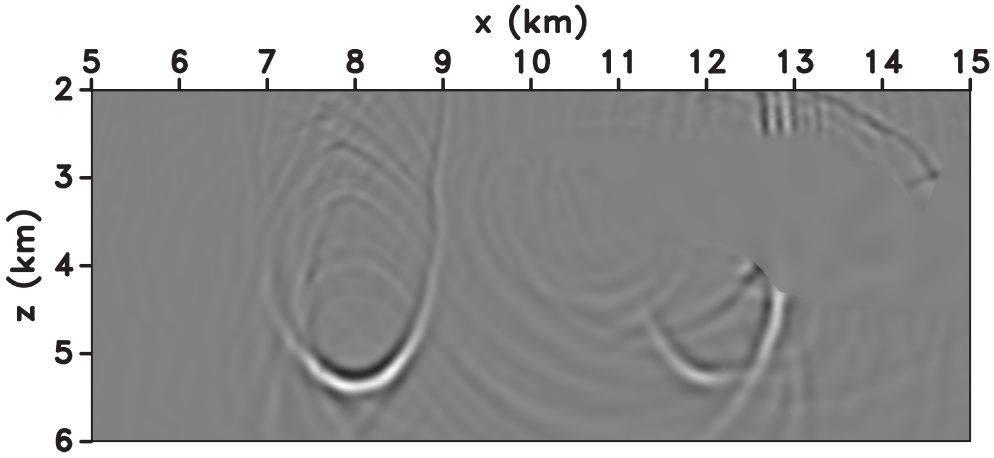
Figure 3.2: (a) The image of a scatterer formed with the whole velocity model 2% too slow, (b) image formed with correct velocity and (c) image with the whole velocity model 2% too fast. Note that for the scatterer on the right, the pattern due to incorrect velocity is harder to interpret than for the scatterer on the left. This is due to the presence of a salt body over right scatterer (Figure 3.1).



(a)



(b)



(c)

Figure 3.3: (a) The image of a scatterer formed with the whole velocity model 10% too slow, (b) image formed with correct velocity and (c) image with the whole velocity model 10% too fast.

by the work of Etgen et al. (2014), who demonstrate how incorrectly picked top of the salt can affect the quality of the image. In this scenario, I use uncertainty related to the salt boundary, with distortions on the order of the dominant seismic wavelength. Analogous to the inclusion scenario, I generate 1001 models with different salt boundaries, select one to represent the true model and to generate data, and form images as samples of the image posterior distribution with the remaining 1000 velocity models.

I use two approaches to quantify the uncertainty of the posterior image. In the first approach, I treat each image pixel independently and form the corresponding amplitude distribution. Based on that, I compute the image mean and its standard deviation, as a proxy for uncertainty. In the second approach, I track the spatial position of the mean image amplitude inside a window representing source location PDF and form the posterior distribution of the microseismic source location.

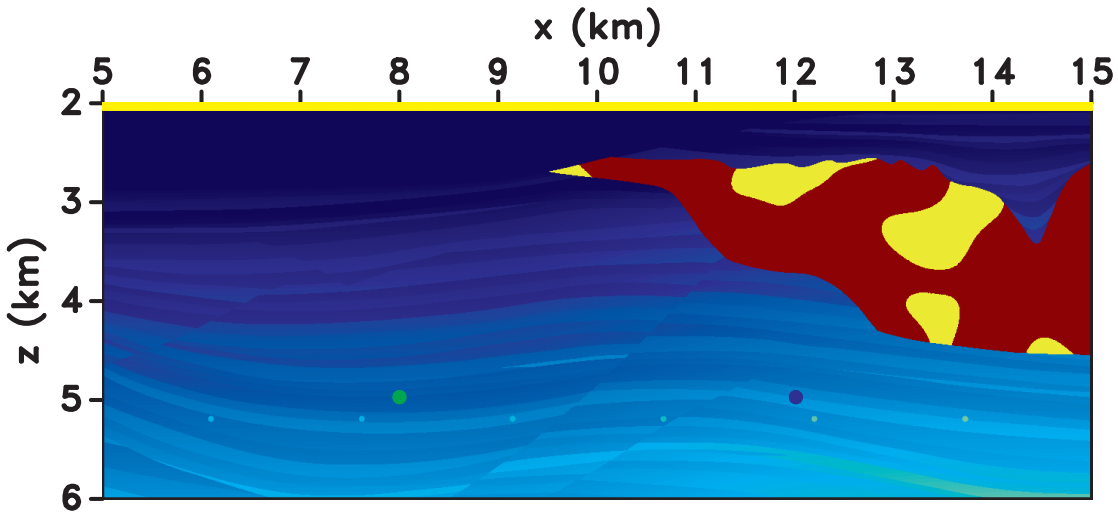
3.2 Methodology

The conceptual simplicity of the Bayesian framework allows one to quantify theoretical uncertainty in a seismic image due to velocity model uncertainty. To meet this objective, I generate data (Figures 3.4(b) and 3.5(b)) using the base models for the salt inclusion and the salt boundary scenarios. The green and blue dots in Figures 3.4(a) and 3.5(a) indicate the location of microseismic sources, while the yellow line on the surface represents a horizontal array of receivers. I form images by backpropagating the data through each of the 1000 velocity models for the given scenario, followed by the cross-correcation with the source wavelet to form an image, according to the equation 3.1:

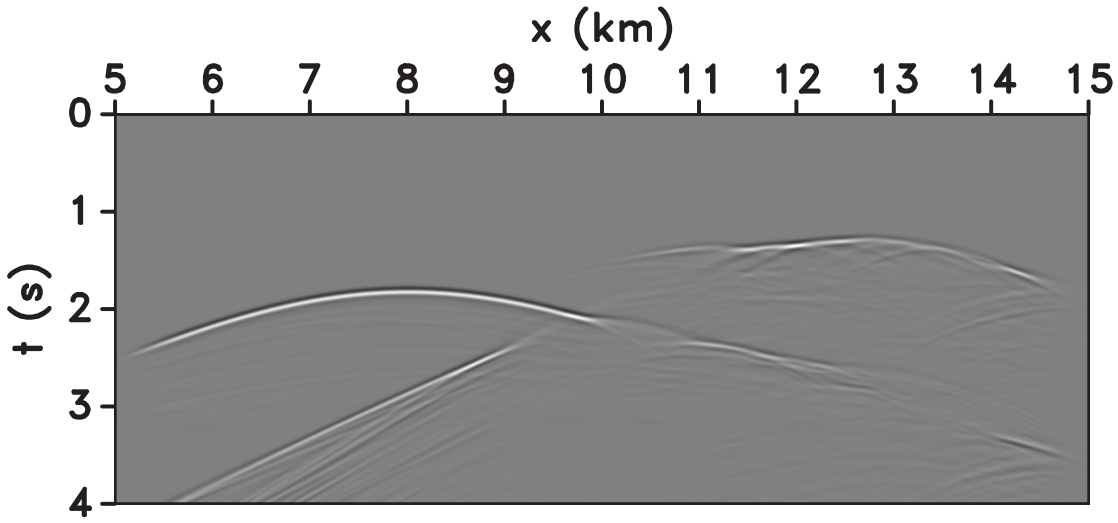
$$I(\mathbf{x}) = \sum_t U(\mathbf{x}, t)\mathrm{w}(t), \tag{3.1}$$

where $I(\mathbf{x})$ is the image at location $\mathbf{x}$, $U(\mathbf{x}, t)$ is the reconstructed wavefield and $\mathrm{w}(t)$ is the source wavelet.

Different realizations of the velocity model in both scenarios have a common geological denominator, but the statistics corresponding to each velocity realization are different. To

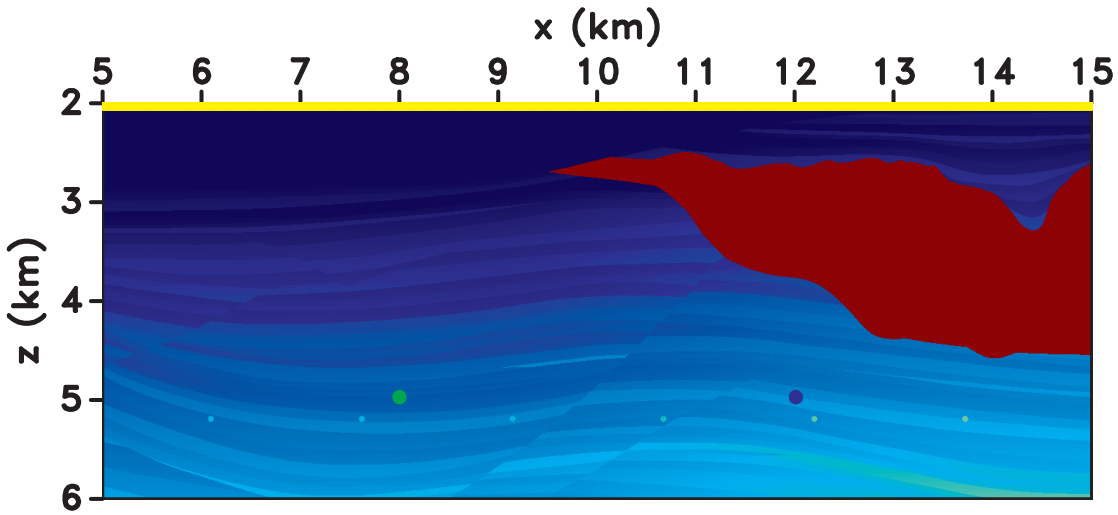


(a)

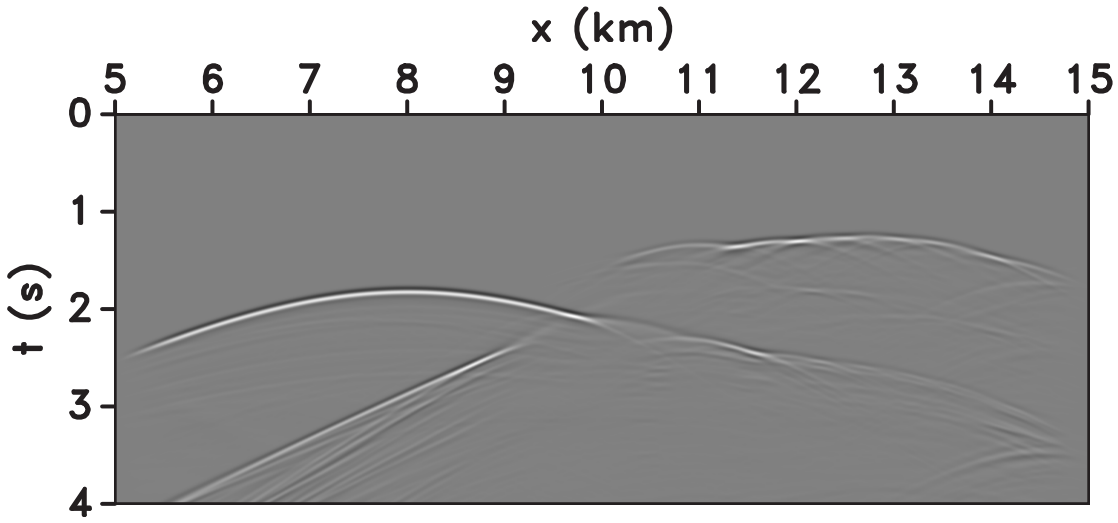


(b)

Figure 3.4: (a) The velocity model used to generate data for the salt inclusion scenario. The yellow line is a line of receivers on the surface. The green and blue dots are subsediment and subsalt sources, respectively. (b) Data generated from the model above used for imaging in the salt inclusion scenario.



(a)



(b)

Figure 3.5: (a) The velocity model used to generate data for the unknown salt boundary scenario. The yellow line is the line of receivers on the surface. The green and blue dots are subsediment and subsalt sources, respectively. (b) Data generated from the model above used for imaging in the salt boundary scenario.

capture that difference, I compute ℓ_2 distances for all velocity differences $\Delta v_i = v_{true} - v_i$, where v_i is one of the 1000 velocity models in each scenarios. Similarly, I compute ℓ_2 distances for all image differences $\Delta I_i = I_{true} - I_i$, where I_i is one of the 1000 images from posterior distribution. Cross-plotting these two quantities captures the character of the relationship between velocity and image, in particular, whether that relationship is linear. The histograms of $\|\Delta v\|_2$ and $\|\Delta I\|_2$ capture the range of distances between true value and each realization.

For every pixel in an image, there are 1000 amplitude values. The histogram of these amplitudes can be converted to an empirical PDF, representing a posterior amplitude distribution. Given this distribution, one can compute a mean and standard deviation at every position, as described in Chapter 1. Using this approach, I describe the image amplitude uncertainty, with standard deviation as a proxy.

The seismic image amplitudes, as defined in this work, do not have a physical meaning, as they are simply a zero-lag cross-correlation of the reconstructed wavefield with the source wavelet. Therefore, the values describing the image uncertainty are not very informative to an interpreter. An alternative is to represent image uncertainty on a normalized scale, which assigns low values to high uncertainty regions and high values to regions with small uncertainty. Such uncertainty representation can be achieved with a linear transform proposed by Li and Sun (2016):

$$c_i = \frac{\sigma_{max} - \sigma_i}{\sigma_{max} - \sigma_{min}}, \tag{3.2}$$

where c_i is the confidence index associated with the i^{th} pixel, and $\sigma_{min}, \sigma_{max}$ and σ_i are the minimum, maximum and i^{th} pixel standard deviations, respectively. The confidence index map does not address the lack of physical units, but it provides an easy way to highlight the uncertain regions of the image.

While the confidence index helps to quantify amplitude uncertainty, it says nothing about the location of the feature of interest. To quantify the location uncertainty, one needs a way of interpreting features and their location from a seismic image. The image of a microseismic source can be characterized by strong amplitudes in the vicinity of the interpreted source

location and very small amplitudes away from that location. I identify the source location by turning the image envelope into a PDF and computing its mean and standard deviation. In this way, the interpreted location takes into account the amplitude information from the whole region around the identified source.

3.3 Image uncertainty

The analysis of image uncertainty provides an insight in three main areas: the relationship between the uncertain velocity and the image, characterized by velocity and image distances, the imprint of velocity uncertainty on a seismic image uncertainty, summarized by standard deviation and confidence index maps, and the uncertainty of the interpreted source location as discussed next. In each subsection below, I present and discuss results relevant to each of these subjects.

3.3.1 Velocity vs image

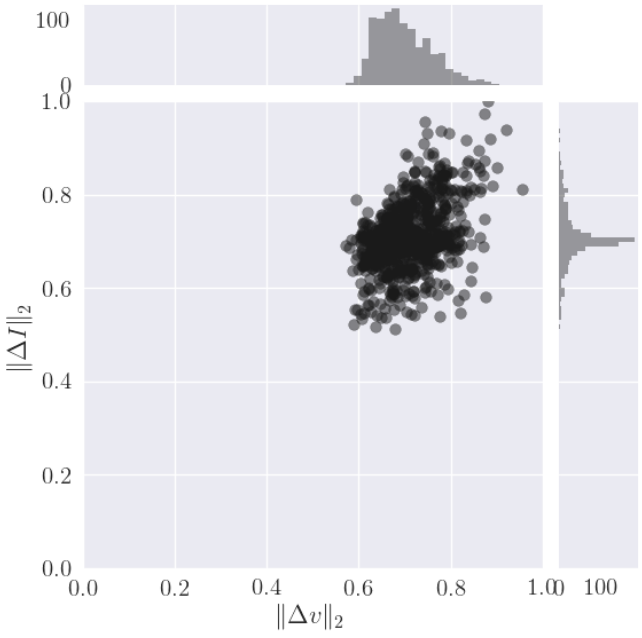


Figure 3.6: ℓ_2 distance of the velocity difference vs ℓ_2 distance of the image difference for the salt inclusion scenario (Figure 3.4). The distances are normalized on a common scale for both scenarios.

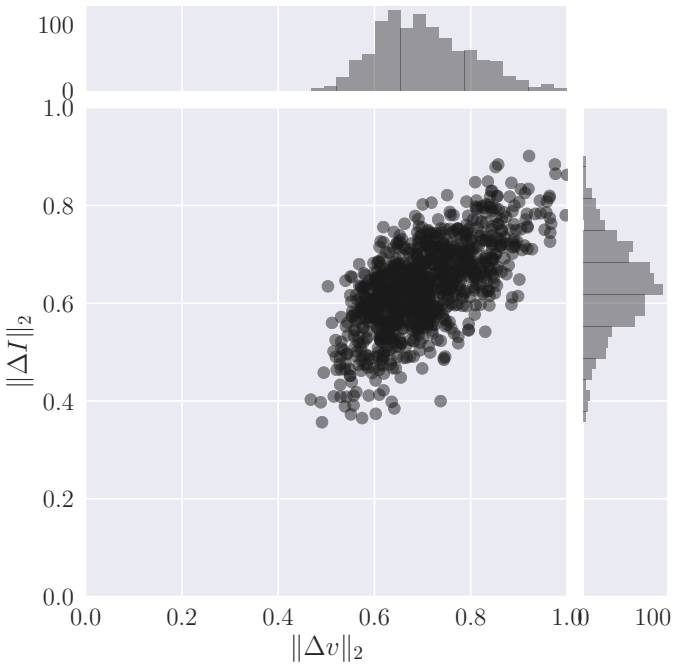


Figure 3.7: ℓ_2 distance of the velocity difference vs ℓ_2 distance of the image difference for the unknown salt boundary scenario (Figure 3.5). The distances are normalized on a common scale for both scenarios.

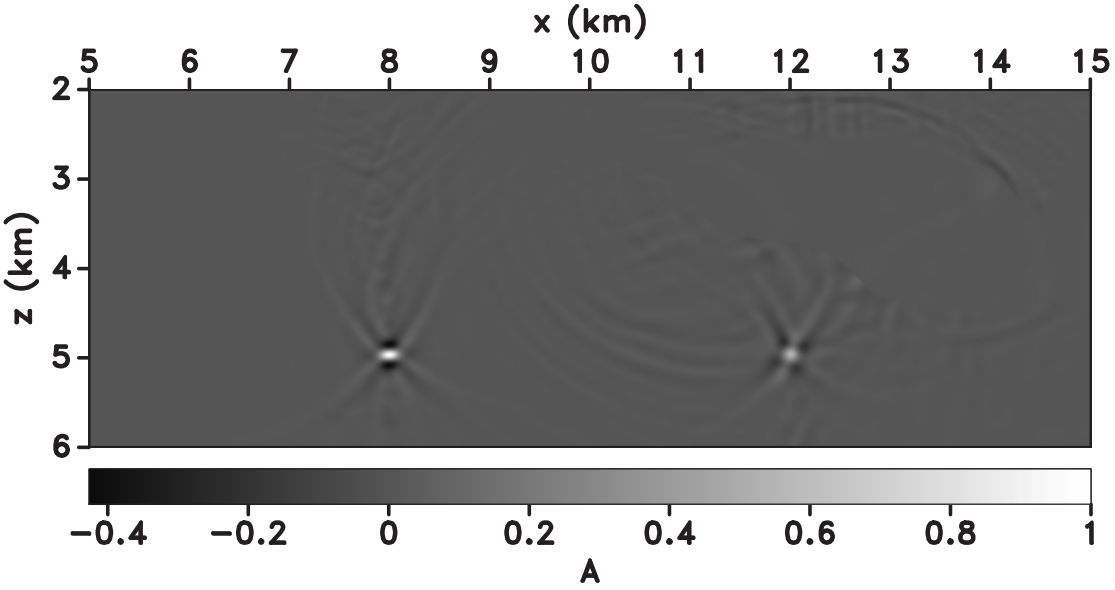
Figures 3.6 and 3.7 show the relationship between the velocity and image distances in the normalized image space. The point cloud is broader for the salt boundary scenario, which is also confirmed by the histograms shown along the ΔI and Δv axes. In the salt inclusion scenario, the image distance is strongly concentrated around the value of about 0.7, indicating that a lot of images share common characteristics. The velocity distance is constrained between 0.6 and 0.8, indicating that velocity and image realizations have a high degree of similarity. The point cloud forms a cluster with no visible directional trend. For the salt boundary scenario, the histograms for velocity and image distance are broader than for salt inclusion scenario, implying higher uncertainty. The scatter plot reveals a weak directional trend. The two scenarios are not well distinguished in the distance space, i.e. if plotted together, many points would overlap, therefore, this plot cannot be used as an uncertainty diagnostic tool.

3.3.2 PDF-based analysis

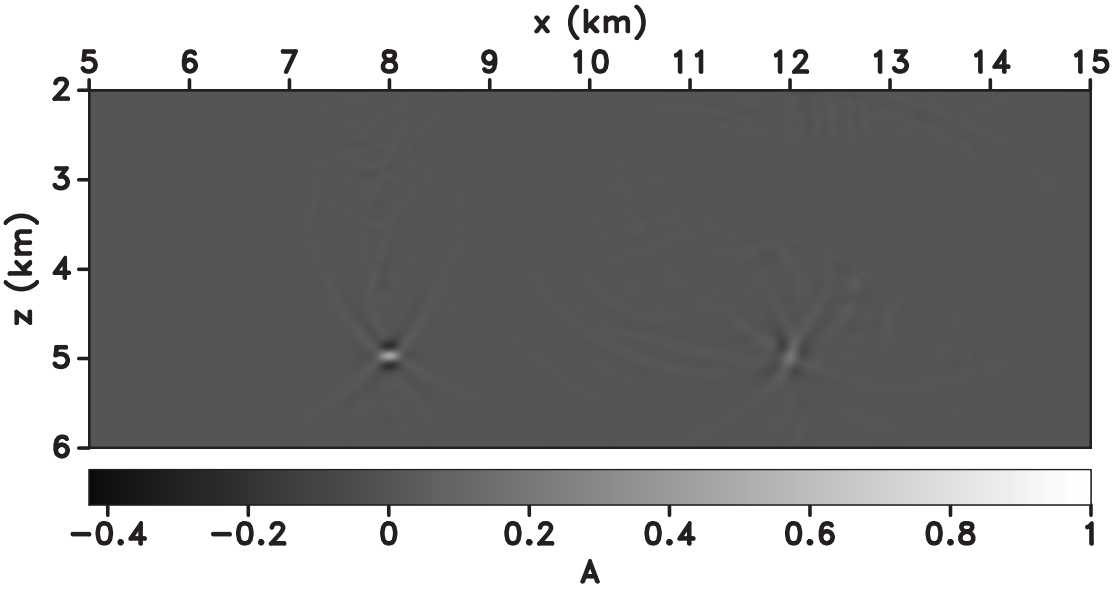
The information about uncertainty is captured in PDFs of image amplitudes. For each scenario, I compute mean and standard deviation, to study the imprint of velocity uncertainty on seismic images. The mean amplitude map represents the center of the posterior image distribution. Contrasted with the true image, it reveals the effect of the velocity uncertainty on the seismic image. First, the amplitudes of images from the posterior are smaller than the amplitudes of the true images. Second, the image of the subsalt source is blurred while the source under the sediments is well-focused (Figures 3.8 and 3.9). The high amplitudes at source locations for the true images are expected, as some velocity estimation techniques rely on the focusing strength to derive velocities. However, recognizing the type of velocity uncertainty by looking at the slightly blurred image for the subsalt source is challenging without some additional geological knowledge. The fact that the same type of velocity uncertainty has smaller effect on the subsediment source is easily explained, as the wavefields generated by that source and registered on the surface propagate mostly through the sediments, and only a small portion is affected by the uncertain salt. Another effect of velocity uncertainty on the mean image amplitude is the attenuation of some strong imaging artifacts visible on true images (e.g. above the salt at x=13.5km and z=2.5km). One possible explanation for this behavior is that artifacts are more sensitive to velocity changes.

Further insight about posterior images can be gained by the study of image amplitude distributions at source locations (Figures 3.10 and 3.11). Note that the distributions for the subsalt source are about two times broader than for the subsediment source and that the distributions for the inclusion scenario are more concentrated around their center. Thus, the boundary scenario is more uncertain, with the highest uncertainty related to the subsalt source.

The image amplitude uncertainty is captured by standard deviation maps (Figures 3.12(a) and 3.13(a)). As expected, the highest uncertainty occurs at the subsalt source, and the standard deviation is greater for the uncertain salt boundary scenario. In the salt inclusion

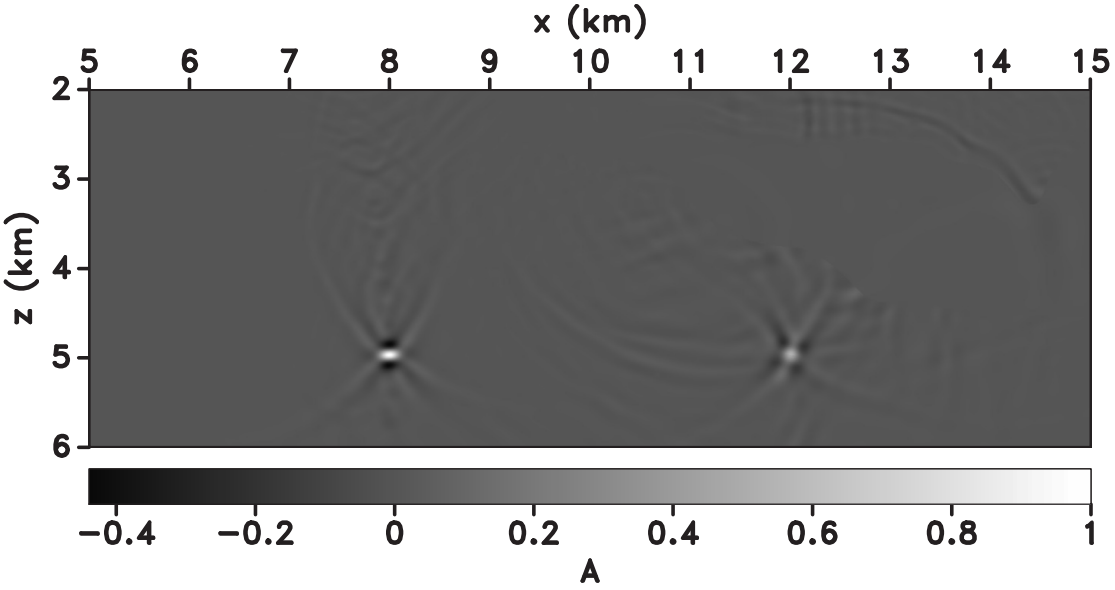


(a)

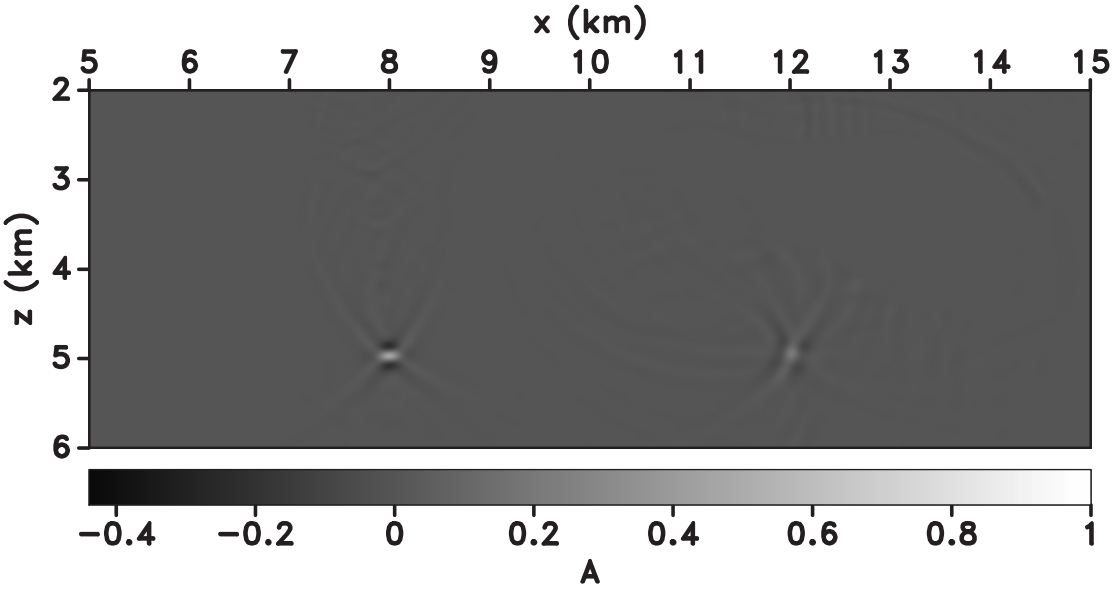


(b)

Figure 3.8: (a) Image generated with the true velocity and (b) the mean image computed from the amplitude PDFs for the salt inclusion scenario.



(a)



(b)

Figure 3.9: (a) Image generated with the true velocity and (b) the mean image computed from the amplitude PDFs for the unknown salt boundary scenario.

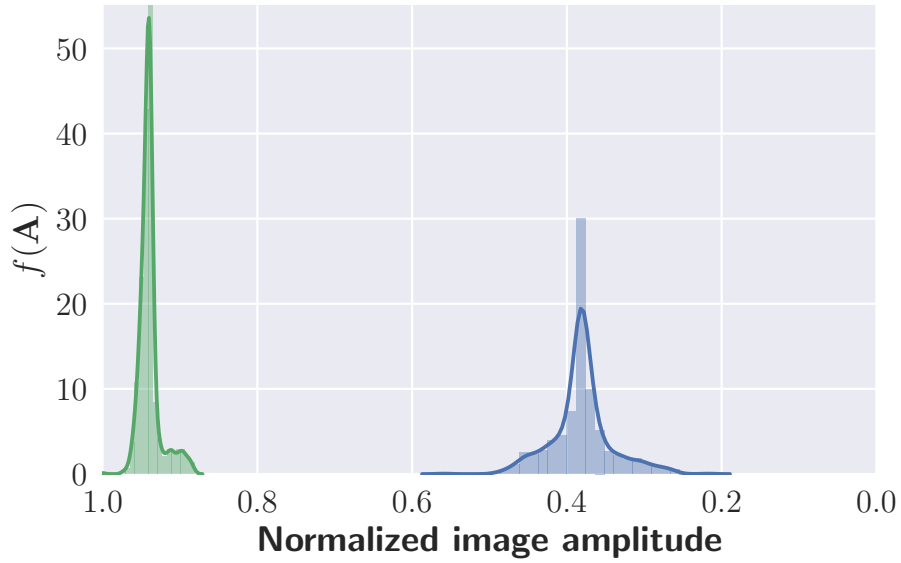


Figure 3.10: PDF of amplitude between 1000 realizations for the subsediment source (green) and the subsalt source (blue) for the salt inclusion scenario. Note that the range of amplitudes is much broader for the subsalt source.

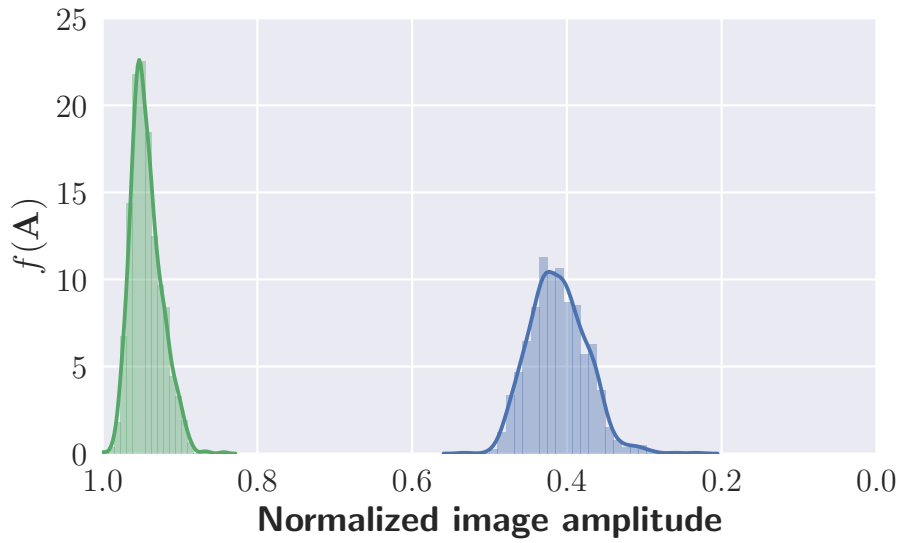


Figure 3.11: PDF of amplitude between 1000 realizations for the subsediment source (green) and the subsalt source (blue) for the unknown salt boundary scenario. Note that the range of amplitudes is much broader for the subsalt source.

scenario, the highest uncertainty follows a trajectory along the salt body while the uncertain region in the salt boundary scenario does not reveal a strong directional trend. This indicates that the salt inclusion scenario creates preferred directions of wave propagation, potentially leading to the illumination gaps.

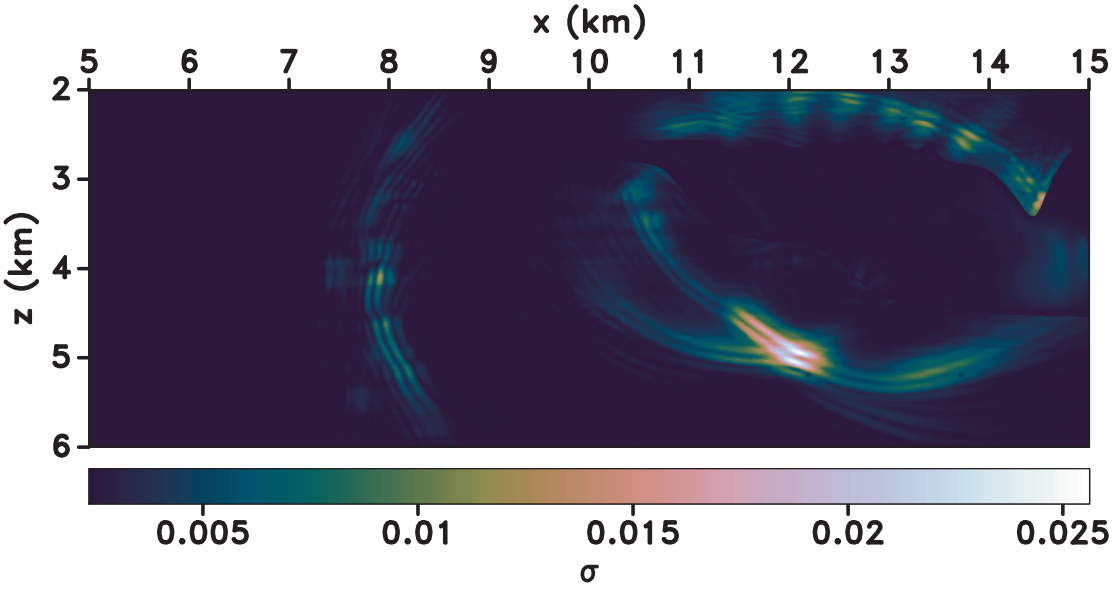
The range of standard deviation values is larger in the uncertain boundary scenario, but these values are not informative to an interpreter. The same information is conveyed on confidence index maps (Figures 3.12(b) and 3.13(b)) using more intuitive scale between 0 (high uncertainty) and 1 (low uncertainty).

3.3.3 Location uncertainty

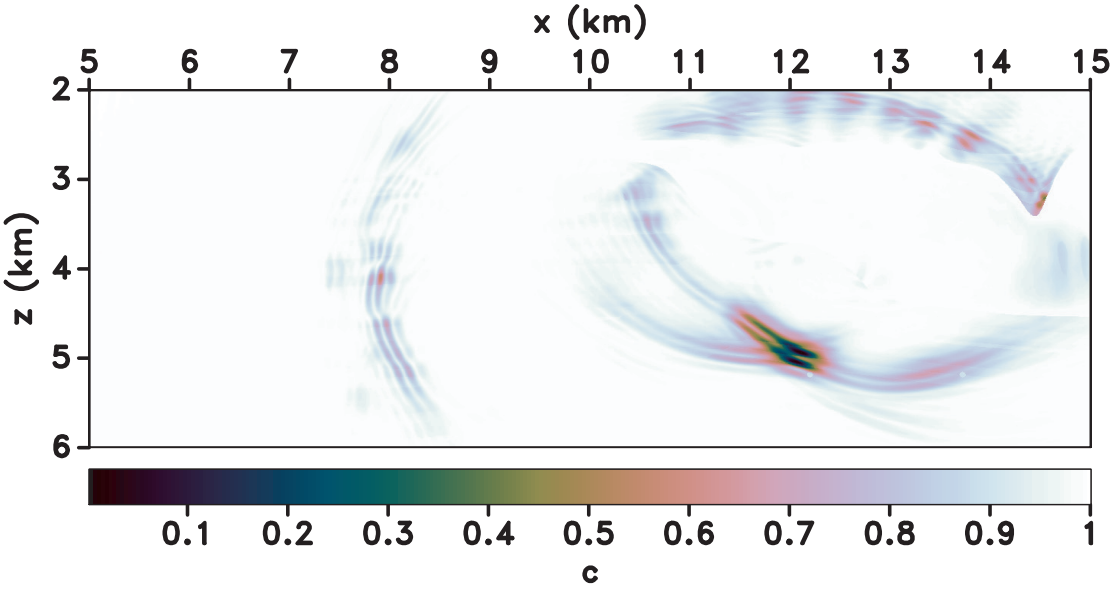
An alternative to capturing microseismic image uncertainty is by quantifying interpreted source location uncertainty (Figures 3.14 and 3.15). The location uncertainty for the subsediment source is smaller than for the subsalt source. The location PFDs not only inform about the location uncertainty values, but also about the well-resolved and poorly-resolved directions. In the salt inclusion scenario, the biggest uncertainty is in the direction parallel to the salt body. In the salt boundary scenario, the highest uncertainty is also along the salt, although the perpendicular direction is only slightly better resolved. Since the acquisition geometry is the same in both scenarios, the observations cannot be explained on the grounds of aperture. These uncertainty patterns are a direct consequence of the velocity uncertainty.

3.4 Discussion and conclusions

The numeric examples demonstrate that it is possible to obtain well-focused images for incorrect velocities. The focusing quality depends on the position of the imaged point. Velocity uncertainty causes wavefield distortion, but at enough distance from the uncertain velocity region, the wavefront heals resulting in focused images. Unlike for inaccurate velocity scaling factor, which results in characteristic smile or frown patterns, velocity uncertainty related to features in the nullspace of the tomographic operator is not easily detectable in

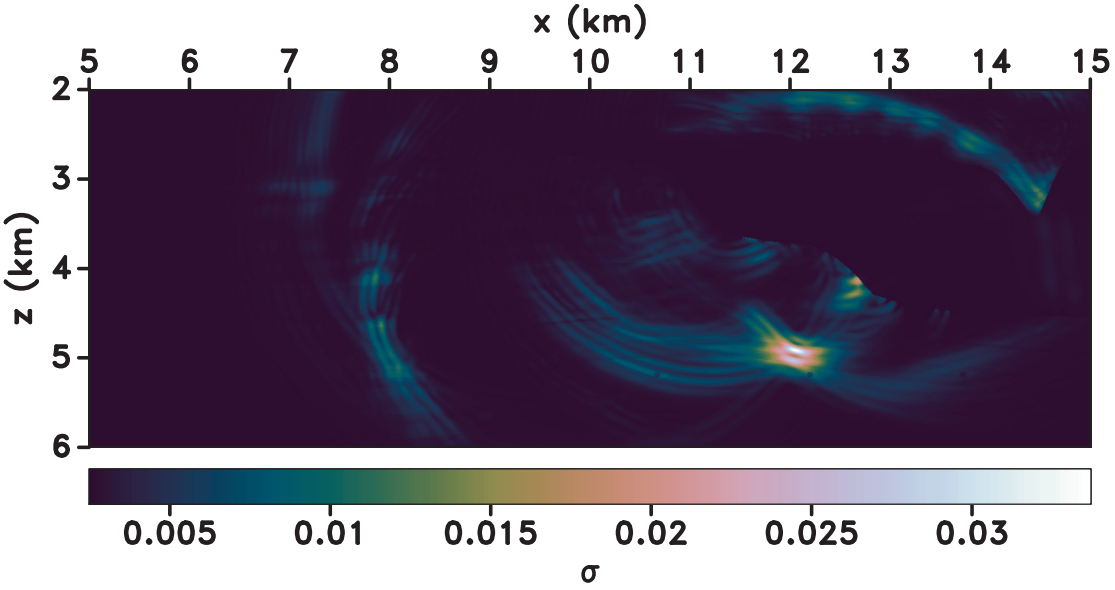


(a)

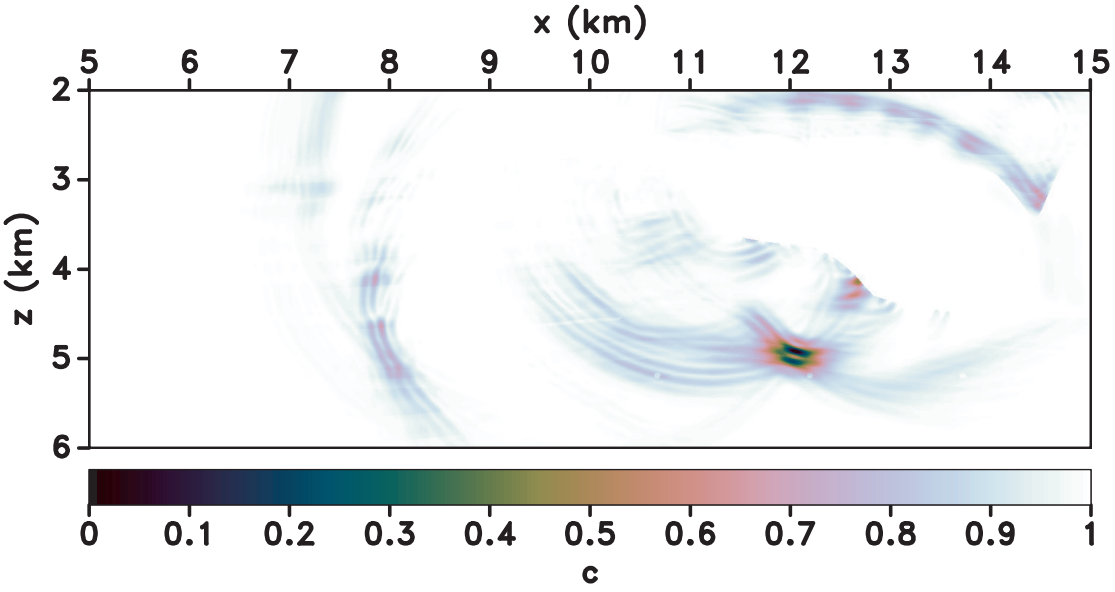


(b)

Figure 3.12: (a) The standard deviation map, computed from 1000 images for the salt inclusion scenario. (b) The confidence index computed using equation 3.2.

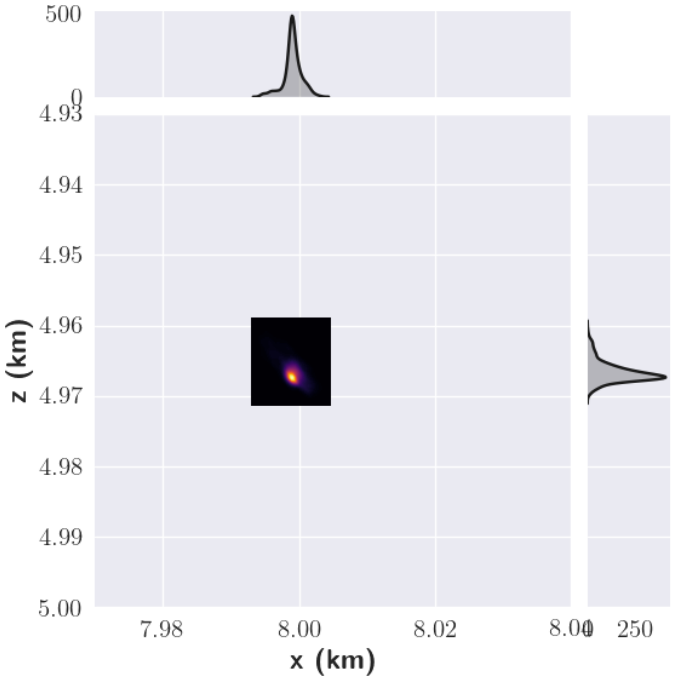


(a)

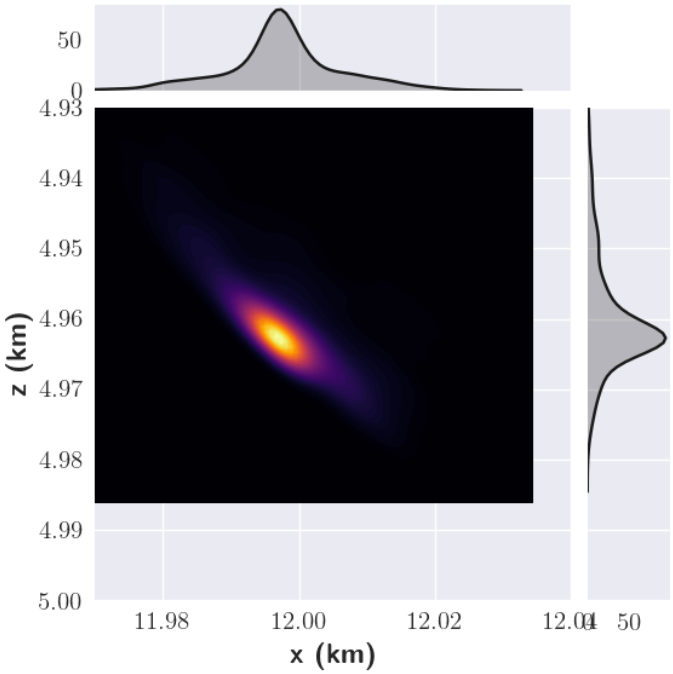


(b)

Figure 3.13: (a) The standard deviation map, computed from 1000 images for the unknown salt boundary scenario. (b) The confidence index computed using equation 3.2.

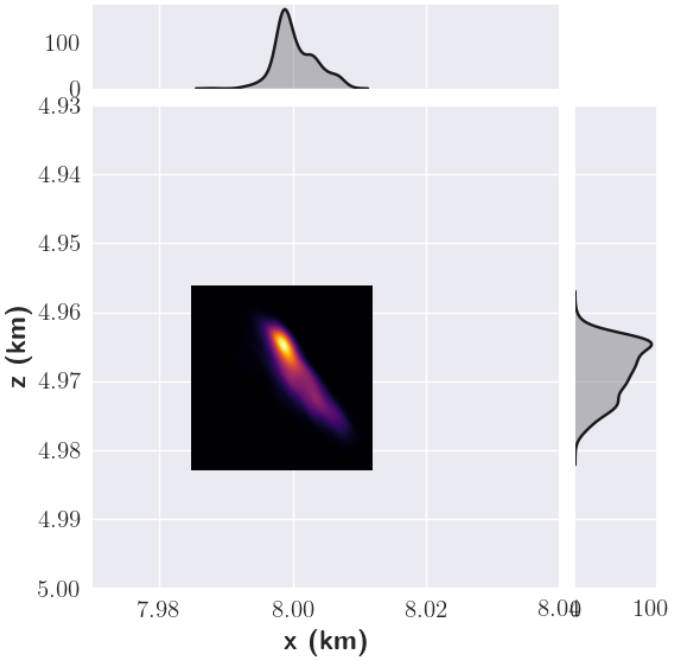


(a)

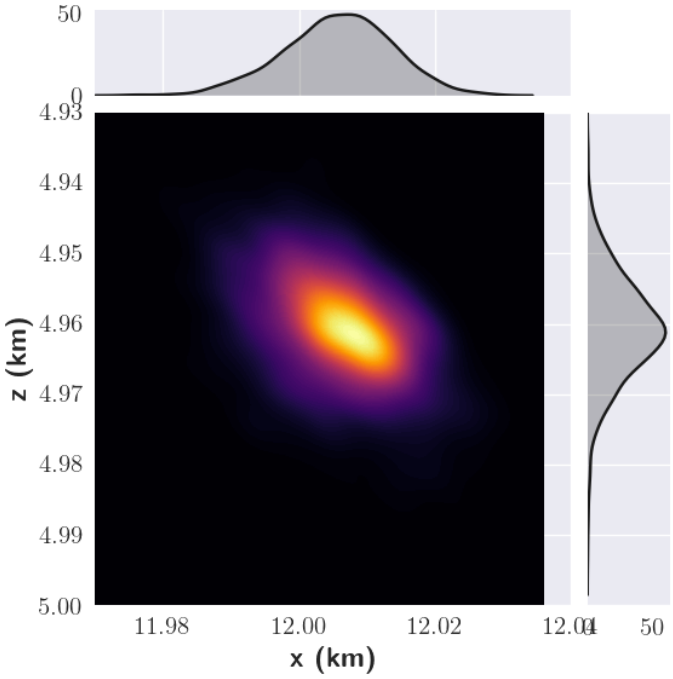


(b)

Figure 3.14: (a) The location PDF corresponding to the source under the sediments and (b) the location PDF corresponding to the source under the salt for the inclusion scenario. Note that (a) is very well constrained to the 12m x 12m region, whereas (b) is broader, occupying 50m x 50m region, so its uncertainty is higher.



(a)



(b)

Figure 3.15: (a) The location PDF corresponding to the source under the sediments and (b) the location PDF corresponding to the source under the salt for the unknown salt boundary scenario. Note that (a) is very well constrained to the 25m x 25m region, whereas (b) is broader, occupying 60m x 60m region, and has higher uncertainty.

the image domain.

The location uncertainty depends both on the source position and the type of velocity uncertainty. Changes to the shape of the salt cause bigger uncertainty than the presence of salt inclusions. Image of the subsalt source is more uncertain because, compared to the subsediment source, a bigger portion of the wavefield excited by this source travels through the uncertain region. However, image uncertainty changes if the acquisition geometry is different. For example, if the aperture is limited such that data not affected by the presence of the salt are unavailable, the effect on the image uncertainty would be more pronounced. The source under the sediments would be illuminated from only one side, and this fact alone would drastically increase the depth uncertainty. The source under the salt would be more defocused and uncertain, because the distorted wavefronts would not heal. Without unaffected data constraining the solution, the uncertainty surrounding the source increases. This highlights the importance of smart acquisition design to account for illumination issues for the subsalt targets.

The confidence index maps are better for interpreting the uncertainty: values close to 1 indicate areas of high confidence while values close to 0 are the most uncertain. We must keep in mind, however, that this confidence relates to image amplitude. The areas of low confidence do not inform about the existence of the image feature, only about the amplitude of that feature. Note that on Figures 3.12(b) and 3.13(b) there are regions (e.g. inside the salt), for which the confidence is high, but without a feature of interest (in this case, no seismic source). The subsediment source is also in the region of high confidence and its imprint is negligible. Conversely, the region around the subsalt source has very low confidence and we observe a pattern that indicates the trajectory along which amplitudes change the most.

While the existence of the seismic source is not in question for the microseismic problem, the subsurface image contains features that are not real. In some cases, they are easily identified but sometimes they may resemble plausible geological structures (for example

faults). Therefore, the ideal final product of uncertainty estimation should give insight into feature existence, along the information about shape and position of the structure. This presents a challenge, since the feature of interest has to be interpreted on every image from the posterior, and the act of interpreting potentially introduces another layer of uncertainty. One possible solution is to introduce an automated, unbiased interpretation tool based on image attributes and use those interpretations as an input to the uncertainty quantification workflow. However, the issue of interpretation uncertainty is not addressed further in this thesis.

CHAPTER 4

CONCLUSIONS AND RECOMMENDATIONS

4.1 Conclusions

Accounting for a long list of uncertainty sources in seismic imaging is challenging because the imaging system is non-linear and different uncertainty sources cannot be studied in complete separation form one another. In an ideal case, one would like to study every uncertainty source independently and to quantify its impact on the image uncertainty. However, there are too many variables in play, including possible *unknown unknowns*, to carry out that task. Consider, for example, the uncertainty related to noisy data. The field data experiments described in Chapter 2 show that data noise is more complicated than one would anticipate. Typically, a seismic trace is described as a convolution of the source wavelet with a reflectivity series, contaminated by additive noise. The convolutional model, however, does not accurately describe the reality of a seismic experiment: there is a clear connection between the strength of a signal and its uncertainty. Yet, repeatability levels computed for two independent systems for the same experiment are comparable, so it is fair to say that the same "flavor" of noise is observed in both. The observed noise patterns, with correlation between uncertainty and the mean amplitude, are likely related to instrument characteristics, such as gain and amplitude response. The answer to the simple question of, "What is the uncertainty of seismic data?" is much more ambiguous than expected due to the fact that the noise model for instrumentation is not well-studied.

The data uncertainty should be translated into the uncertainty of seismic images. However, data are processed prior to imaging and raw data uncertainty is different from the uncertainty of processed data. To be thorough, one should keep track of how uncertainty levels change during processing, and then use the uncertainty of processed data as an input to imaging. Not accounting for data uncertainty in imaging may lead to inaccurate inter-

pretations (such as fake structures or fake bright spots), which can be avoided if one fully exploits the uncertainty map. Furthermore, information about data distributions and uncertainty can be used to constrain the solutions of inverse problems by guiding the choice of regularization parameters or using full information about distributions as prior knowledge.

Another complication for the seismic image uncertainty quantification is the fact that some processing steps (such as static corrections or spherical divergence correction), require knowledge of the medium properties, which are estimated from the same uncertain seismic data. One such property, with a large impact on the seismic image, is the medium velocity. Velocities derived from seismic data are uncertain, for multiple reasons. First, data are uncertain, second, the tomographic operator can typically only resolve features larger than the dominant wavelength, and third, the acquisition geometry also plays a role, as some regions may not be illuminated sufficiently to be resolved well, simply because not enough energy penetrates to that portion of the subsurface due to the geologic structure or because the aperture is not wide enough to capture all the reflections.

The velocity uncertainty has a large impact on the quality and uncertainty of the seismic image. However, recognizing that an image is formed with an uncertain velocity may be challenging. Chapter 3 shows that, broadly inaccurate velocity causes characteristic smile or frown patterns. In contrast, the impact of local velocity uncertainty on the focused seismic image may be challenging to recognize. In general, the larger the model complexity, the more difficult it is to identify the type of velocity uncertainty by simple analysis of the image. For example, can one always recognize broadly inaccurate velocity? Or distinguish between uncertain salt boundaries and the presence of salt inclusions? In most cases, identifying the type of velocity uncertainty from a seismic image can pose a challenge, especially if features in the effective nullspace of the tomographic operator are present.

An important consideration for uncertainty quantification is its utility. Who is the recipient of the uncertainty map? What image attribute is of interest to them? How does one communicate the uncertainty in the most meaningful way? For example, the uncertainty of

feature location is of interest to people evaluating a prospect. First, the location and the spatial extent of structures directly affect decisions about the placement of wells. Second, the location uncertainty can be easily translated into uncertainty in volume (for example, thickness of the hydrocarbon bearing layer), which impacts economic decisions about the future of a prospect. In contrast, the uncertainty in image amplitudes can offer valuable insight about the concentration of hydrocarbons and other quantities derived from the amplitude attributes. Therefore, the image amplitude uncertainty map is valuable for interpretations based on amplitude attributes.

Once it is clear what image feature is uncertain, one has to determine the most appropriate proxy for characterizing the uncertainty of that feature. This choice is influenced by the size of the problem and by the type of information one seeks. Ideally, the proxy of choice informs about the magnitude and orientation of the uncertainty in the uncertain parameter space. A natural choice for this purpose is the covariance matrix; however, for large problems, it cannot be formed explicitly. A standard deviation map is easier to obtain. Although standard deviation informs only about the magnitude of the uncertainty, the standard deviation map can also provide insight into the spatial orientation of uncertainty, as demonstrated in Chapter 3. The confidence index map, obtained by the linear transformation of the standard deviation map, conveys the same information as standard deviation, but in the easier to interpret normalized scale. For isolated features, such as point scatterers or microseismic sources, the uncertainty can be captured by the location PDF of that feature, since there are only three unknown spatial parameters, and thus the PDF is easy to visualize and interpret.

4.2 Recommendations

The biggest challenges to imaging uncertainty quantification are accounting for all uncertainty sources, reducing the dimensionality of the problem and decreasing the computational cost. There are several mechanisms that could help to address these challenges.

One idea is to design data acquisition such as to gather less data while preserving the overall information that could be inferred from them. With nodal acquisition systems, it is possible to design surveys with an element of randomness in surface sampling, which would allow to recover full information with less samples than required by the Nyquist?s sampling criterion. This idea is advocated by Herrmann (2010), who illustrates its utility by a number of case studies. Such acquisition setups could also potentially help with noise attenuation, especially on land, by turning coherent, correlated noise to something that looks more random, and thus is easier to remove.

Another way of reducing the dimensionality of the problem could exploit the structure underlying the models and find their sparsest representation, e.g. by describing their spatial correlations through variograms. If one could describe a complex, 3D velocity model with tens of parameters instead of thousands of parameters, the uncertainty in both velocity and image would be easier to quantify (with less parameters, the computational time is significantly reduced and one may explore more samples from the posterior). Furthermore, using prior knowledge about model structure allows to reduce the uncertainty. Conceptually, invoking knowledge about model structure is equivalent to imposing a prior model PDF that is narrower (i.e. has smaller uncertainty) than the prior model PDF without such constraints. Consequently, the posterior model also has smaller uncertainty. Unfortunately, finding a sparse representation for a complicated 3D model is challenging and requires good prior knowledge about the model from sources independent of seismic data.

Finally, the computational cost could be reduced by designing a more efficient, cheaper modeling algorithm. Candes and Demanet (2005) demonstrate that a wave propagator written in the curvelet domain is optimally sparse, with substantial reduction in cost compared to the traditional finite-differences modeling. However, it remains for future research to evaluate whether curvelets could provide a sparse representation of wavefields in complex geological settings.

REFERENCES CITED

Anderson, T. W., 1958, An introduction to multivariate statistical analysis: Wiley.

Avseth, P., T. Mukerji, and G. Mavko, 2010, Quantitative seismic interpretation: Applying rock physics tools to reduce interpretation risk: Cambridge University Press.

Baysal, E., D. D. Kosloff, and J. W. Sherwood, 1983, Reverse time migration: Geophysics, **48**, 1514–1524.

Berkhout, A. J., 2012, Seismic migration: Imaging of acoustic energy by wave field extrapolation: Elsevier, **12**.

Bishop, T., K. Bube, R. Cutler, R. Langan, P. Love, J. Resnick, R. Shuey, D. Spindler, and H. Wyld, 1985, Tomographic determination of velocity and depth in laterally varying media: Geophysics, **50**, 903–923.

Biswas, R., and M. Sen, 2017, 2d Full-Waveform Inversion and uncertainty estimation using the Reversible Jump Hamiltonian Monte Carlo, *in* SEG Technical Program Expanded Abstracts 2017: Society of Exploration Geophysicists, 1280–1285.

Buland, A., O. Kolbjørnsen, and A. J. Carter, 2011, Bayesian Dix inversion: Geophysics, **76**, R15–R22.

Candes, E. J., and L. Demanet, 2005, The curvelet representation of wave propagators is optimally sparse: Communications on Pure and Applied Mathematics, **58**, 1472–1528.

Claerbout, J. F., and S. M. Doherty, 1972, Downward continuation of moveout-corrected seismograms: Geophysics, **37**, 741–768.

Dix, C. H., 1955, Seismic velocities from surface measurements: Geophysics, **20**, 68–86.

Duijndam, A., 1988, Bayesian estimation in seismic inversion. Part II: Uncertainty analysis: Geophysical Prospecting, **36**, 899–918.

Ely, G., A. Malcolm, and O. V. Poliannikov, 2018, Assessing uncertainties in velocity models and images with a fast nonlinear uncertainty quantification method: Geophysics, **83**, R63–R75.

Etgen, J. T., I. Ahmed, and M. Zhou, 2014, Seismic adaptive optics, *in* SEG Technical Program Expanded Abstracts 2014: Society of Exploration Geophysicists, 4411–4415.

Fang, Z., F. J. Herrmann, and C. D. Silva, 2014, Fast uncertainty quantification for 2D full-waveform inversion with randomized source subsampling: Presented at the 76th EAGE Conference and Exhibition 2014.

Freeman, B., P. J. Boult, G. Yielding, and S. Menpes, 2010, Using empirical geological rules to reduce structural uncertainty in seismic interpretation of faults: Journal of Structural Geology, **32**, 1668–1676.

Gouveia, W. P., and J. A. Scales, 1998, Bayesian seismic waveform inversion: Parameter estimation and uncertainty analysis: Journal of Geophysical Research: Solid Earth, **103**, 2759–2779.

Gray, S. H., J. Etgen, J. Dellinger, and D. Whitmore, 2001, Seismic migration problems and solutions: Geophysics, **66**, 1622–1640.

Gray, S. H., and W. P. May, 1994, Kirchhoff migration using eikonal equation traveltimes: Geophysics, **59**, 810–817.

Hajnal, Z., and I. Sereda, 1981, Maximum uncertainty of interval velocity estimates: Geophysics, **46**, 1543–1547.

Herrmann, F. J., 2010, Randomized sampling and sparsity: Getting more information from fewer samples: Geophysics, **75**, WB173–WB187.

Hill, N. R., 1990, Gaussian beam migration: Geophysics, **55**, 1416–1428.

———, 2001, Prestack Gaussian-beam depth migration: Geophysics, **66**, 1240–1250.

Houck, R. T., 2007, Time-lapse seismic repeatability - How much is enough?: The Leading Edge, **26**, 828–834.

Hughes, J. K., 1998, Examination of seismic repeatability as a key element of time-lapse seismic monitoring: Presented at the European Petroleum Conference, Society of Petroleum Engineers.

Irakarama, M., P. Cupillard, G. Caumon, and P. Sava, 2017, Appraising structural models using seismic data: problem and challenges, *in* SEG Technical Program Expanded Abstracts 2017: Society of Exploration Geophysicists, 1897–1901.

Jannane, M., W. Beydoun, E. Crase, D. Cao, Z. Koren, E. Landa, M. Mendes, A. Pica, M. Noble, G. Roeth, S. Singh, R. Snieder, A. Tarantola, D. Trezeguet, and M. Xie, 1989, Wavelengths of earth structures that can be resolved from seismic reflection data: Geophysics, **54**, 906–910.

Kragh, E., and P. Christie, 2002, Seismic repeatability, normalized RMS, and predictability: The Leading Edge, **21**, 640–647.

Landa, E., P. Thore, V. Sorin, and Z. Koren, 1991, Interpretation of velocity estimates from coherency inversion: Geophysics, **56**, 1377–1383.

Landrø, M., 1999, Repeatability issues of 3-D VSP data: Geophysics, **64**, 1673–1679.

———, 2001, Discrimination between pressure and fluid saturation changes from time-lapse seismic data: Geophysics, **66**, 836–844.

Larner, K., and C. Beasley, 1987, Cascaded migrations: Improving the accuracy of finite-difference migration: Geophysics, **52**, 618–643.

Lee, T.-W., 1998, Independent component analysis, *in* Independent Component Analysis: Springer, 27–66.

Levin, S. A., 1984, Principle of reverse-time migration: Geophysics, **49**, 581–583.

Li, Y., and J. Sun, 2016, 3d magnetization inversion using fuzzy c-means clustering with application to geology differentiation: Geophysics, **81**, J61–J78.

Loewenthal, D., and I. R. Mufti, 1983, Reversed time migration in spatial frequency domain: Geophysics, **48**, 627–635.

Lombardi, O., F. Holik, and L. Vanni, 2016, What is Shannon information?: Synthese, **193**, 1983–2012.

Lumley, D. E., 2001, Time-lapse seismic reservoir monitoring: Geophysics, **66**, 50–53.

McMechan, G. A., 1983, Migration by extrapolation of time-dependent boundary values: Geophysical Prospecting, **31**, 413–420.

Naess, O. E., 2006, Repeatability and 4D seismic acquisition, *in* SEG Technical Program Expanded Abstracts 2006: Society of Exploration Geophysicists, 3300–3304.

Osypov, K., D. Nichols, M. Woodward, O. Zdraveva, and C. Yarman, 2008, Uncertainty and resolution analysis for anisotropic tomography using iterative eigendecomposition, *in* SEG Technical Program Expanded Abstracts 2008: Society of Exploration Geophysicists, 3244–3249.

Osypov, K., Y. Yang, A. Fournier, N. Ivanova, R. Bachrach, C. E. Yarman, Y. You, D. Nichols, and M. Woodward, 2013, Model-uncertainty quantification in seismic tomography: Method and applications: Geophysical Prospecting, **61**, 1114–1134.

Poggiagliolmi, E., L. Wouters, N. Ondraf, and M. Verkeyn, 1998, Time-lapse seismic repeatability a case study, *in* SEG Technical Program Expanded Abstracts 1998: Society of Exploration Geophysicists, 12–15.

Pratt, R. G., 1999, Seismic waveform inversion in the frequency domain, part 1: Theory and verification in a physical scale model: Geophysics, **64**, 888–901.

Rapstine, T., Y. Li, and J. Sun, 2016, Integrating a spatial salt likelihood map and prior petrophysical data into a gravity gradiometry inversion through fuzzy c-means clustering: Presented at the SEG Technical Program Expanded Abstracts 2016, Society of Exploration Geophysicists.

Rawlinson, N., A. Fichtner, M. Sambridge, and M. K. Young, 2014, Seismic tomography and the assessment of uncertainty, *in* Advances in Geophysics: Elsevier, **55**, 1–76.

Shannon, C. E., 1948, A mathematical theory of communication: Bell system technical journal, **27**, 379–423.

Stolt, R., 1978, Migration by Fourier transform: Geophysics, **43**, 23–48.

Sullivan, T. J., 2015, Introduction to uncertainty quantification: Springer, **63**.

Tarantola, A., 1984, Inversion of seismic reflection data in the acoustic approximation: Geophysics, **49**, 1259–1266.

———, 2005, Inverse problem theory and methods for model parameter estimation: SIAM, **89**.

Tarantola, A., and B. Valette, 1982a, Generalized nonlinear inverse problems solved using the least squares criterion: Reviews of Geophysics, **20**, 219–232.

———, 1982b, Inverse problems = quest for information: Journal of Geophysics, **50**, 150–170.

Thore, P., A. Shtuka, M. Lecour, T. Ait-Ettajer, and R. Cognot, 2002, Structural uncertainties: Determination, management, and applications: Geophysics, **67**, 840–852.

Verschuur, D., and A. Berkhout, 2011, Seismic migration of blended shot records with surface-related multiple scattering: Geophysics, **76**, A7–A13.

Virieux, J., and S. Operto, 2009, An overview of full-waveform inversion in exploration geophysics: Geophysics, **74**, WCC1–WCC26.

Xue, Z., Y. Chen, S. Fomel, and J. Sun, 2015, Seismic imaging of incomplete data and simultaneous-source data using least-squares reverse time migration with shaping regularization: Geophysics, **81**, S11–S20.

Yilmaz, O., 2017, Circumventing velocity uncertainty in imaging complex structures, *in* SEG Technical Program Expanded Abstracts 2017: Society of Exploration Geophysicists, 5706–5710.

Zhou, Z., X. Jia, and X. Qiang, 2018, GPU-accelerated element-free reverse-time migration with Gauss points partition: Journal of Geophysics and Engineering, **15**, 718.

Zhu, H., S. Li, S. Fomel, G. Stadler, and O. Ghattas, 2016, A Bayesian approach to estimate uncertainty for full-waveform inversion using a priori information from depth migration: Geophysics, **81**, R307–R323.